MODERATELY POROUS ZIRCONIA CERAMICS FOR DENTAL APPLICATIONS

Sebastjan Perko

Doctoral Dissertation

Jozef Stefan International Postgraduate School

Ljubljana, Slovenia, April 2012

Evaluation Board:

Prof. Dr. Darko Makovec, Chairman, Jozef Stefan Institute, Jamova 39, SI-1000 Ljubljana

Prof. Dr. Marija Kosec, Member, Jozef Stefan Institute, Jamova 39, SI-1000 Ljubljana

Prof. Dr. Mihael Drofenik, Member, University of Maribor, Faculty of chemistry and chemical engineering, Smetanova 17, SI-2000 Maribor

MEDNARODNA PODIPLOMSKA ŠOLA JOŽEFA STEFANA
JOŽEF STEFAN INTERNATIONAL POSTGRADUATE SCHOOL

Sebastjan Perko

MODERATELY POROUS ZIRCONIA CERAMICS FOR DENTAL APPLICATIONS

Doctoral Dissertation

ZMERNO POROZNA CIRKONIJEVA OKSIDNA KERAMIKA ZA DENTALNE NAMENE

Doktorska disertacija

Supervisor: Prof. Dr. Tomaž Kosmač

Co-Supervisor: Dr. Aleš Dakskobler

Ljubljana, Slovenia, April 2012

Table of Contents

Abstract

This doctoral thesis describes the preparation of moderately porous Y-TZP ceramics with improved flexural strength. The main field of application is dentistry, where the elastic mismatch between the Y-TZP material and tooth substance influences the survival rate of fixed partial dentures (FPDs). By introducing porosity into the bulk samples a reasonable reduction in the elastic modulus (E) can be expected, as shown by many literature data. A major drawback in using this approach is that the flexural strength of the ceramics is also greatly reduced. The problem was tackled by approaching four major topics in materials science, i.e., colloidal processing, shaping, sintering and mechanical properties.

The first part of the work focused on the colloidal processing. The so-called, core-shell concept was adopted for the preparation of the starting materials. This concept exploits agglomeration, which results in a uniform distribution of nano-sized particles attached to the surface of the submicron-sized particles in the slurry. After the slip casting, the green pellets were biscuit-sintered at various temperatures in the ambient air in order to obtain moderately porous zirconia samples. In the second part, the densification behavior of the bimodal Y-TZP powder compacts consisting of nano/sub-micron-sized particles was studied and an explanation for their improved flexural strength when biscuit-sintered is provided. An in-situ-heating TEM analysis revealed that up to 800 °C only the nanoparticles sinter in a bimodal mixture without any densification. By increasing the temperature to 900 °C the densification of the nanoparticles begins and the partially densified nanoparticle clusters migrate into the contact area between the core particles. Consequently, the driving force for the sintering of the powder-blend compacts is reduced and this is reflected in a slower densification compared to that of the core material. At 1000 °C the sintered nanoparticle clusters begin to incorporate into the core material, resulting in a sharp increase in strength due to the increased neck area. The biscuit-sintered powder-blend compacts reached a plateau of strength at 670 MPa, which was achieved at a relative density of 70 %.

Povzetek

Z doktorskim delom smo poskušali pripraviti zmerno porozno Y-TZP keramiko z izboljšano zlomno trdnostjo. Glavna aplikacija tako modificirane keramike je zobozdravstvo, kjer neujemanje elastičnih lastnosti med gosto sintranim Y-TZP materialom in zobno substanco vpliva na preživetje mostičkov v ustni votlini. Uvajanje poroznosti v "bulk" material ima za posledico zmanjšanje elastičnega modula (E), kar je dobro opisano v literaturi. Neizogibno se s tem pristopom zmanjša tudi zlomna trdnost, kar pa smo reševali v štirih tematskih sklopih, t.j. s koloidnim procesiranjem, oblikovanjem, sintranjem in študijem mehanskih lastnosti.

V prvem delu smo se posvetili koloidnemu procesiranju. Za pripravo izhodnih materialov smo uporabili t.i. "core-shell" koncept, ki temelji na aglomeraciji. S tem pristopom dobimo enakomerno porazdelitev nano-delcev, ki so pripeti na površino sub-mikronskih delcev v suspenziji. Po oblikovanju z nalivanjem, smo vzorce delno sintrali pri različnih končnih temperaturah v zraku tako, da smo dobili zmerno porozne Y-TZP vzorce. V drugem delu smo preučili zgoščevanje take bi-modalne mešanice Y-TZP materiala in podali razlago o izboljšani zlomni trdnosti. In-situ segrevalna TEM analiza nam pove, da se do 800 °C sintrajo samo nano-delci brez zgoščevanja. S povišanjem temperature do 900 °C spodbudimo zgoščevanje med nanodelci, hkrati pa se delno zgoščeni skupki nanodelcev pomikajo v kontaktna področja med dvema sub-mikronskima delcema. S tem pojavom se gonilna sila za sintranje sub-mikronskih delcev zmanjša, kar se odraža na upočasnjenem zgoščevanju v primerjavi s samo sub-mikronskimi delci. Pri 1000 °C se tako premaknjeni skupki nanodelcev začnejo vgrajevati tudi v sub-mikronske delce, kar se odraža z naglim povečanjem zlomne trdnosti, ki je posledica povečane površine vratov med sub-mikronskimi delci. Vzorci sintrani do 70 % teoretične gostote so dosegli plato v zlomni trdnosti pri 670 MPa.

Abbreviations

CRH = constant rate of heating

DCC = direct coagulation casting

DLVO = Derjaguin, Landau, Verwey, Overbeek

E = elastic modulus

GC = gel casting

HAS = hydrolysis-assisted solidification

HHF = Hogg, Heally and Furstenau

IEP = isoeletric point

IM = injection moulding

IUPAC = international union of pure and applied chemistry

LbL = layer by layer

MeOH = metal hydroxide

PZC = point of zero charge

SEM = scanning electron microscopy

SPS = spark plasma sintering

TD = theoretical density

TEM = transmission electron microscopy

Y-TZP = yttria - tetragonal zirconia polycrystal

TZ-3YB = yttria - tetragonal zirconia polycrystal intended for dry-pressing

TZ-3Y(CA) = citric-acid-coated core particles after milling

1 Introduction

1.1 Porous ceramics/materials

Porous materials represent a combination of a controlled void space with an engineering structure for applications ranging from self-lubricating bearings to surgical implants. Porous materials are classified into several types, depending on their respective pore size. According to the IUPAC definition,[1] microporous materials have pore diameters of less than 2 nm, mesoporous materials have pore diameters between 2 nm and 50 nm and macroporous materials have pore diameters greater than 50 nm. Microporous materials are often used in laboratory environments to facilitate contaminant-free exchange of gases. Mold spores, bacteria, and other airborne contaminants become trapped, while allowing gases to pass through the material, so ensuring a sterile working area. Typical mesoporous materials include zeolites, which have similarly sized, fine mesopores[2]. Mesoporous oxides of niobium, tantalum, titanium, zirconium, cerium and tin have also been reported. According to the IUPAC definition, a mesoporous material can be disordered or ordered in a mesostructure. The first mesoporous material with a long-range order was reported in 1990 by Japanese researchers[3]. Around that time, the synthesis was also conducted by a group of the former Mobil Oil Company[4,5]. The use of macroporous ceramics, on the other hand, spans from traditional applications like roof tiles and concrete to advanced technical ceramics in medicine and automobile engines [6,7,8]. Cellular ceramics constitute a specific class of materials with a porosity of > 60 %. They are characterized by the presence of a recognizable cell that is defined as space-possessing faces and solid edges, where the faces can be fully solid or void, giving a closed-cell or an open-cell material, respectively[9].

1.2 Applications

Porous ceramics are desirable for a wide variety of applications. As ceramics, such materials can withstand relatively high temperatures before their degradation or decomposition occurs. A porous body is lighter in weight compared to its dense counterpart; therefore, porous materials are nowadays used in several technological processes and as the end products in many applications. Depending on their nature and the structure of the porosity, typical and novel applications include: the filtration of molten metals or particles from exhaust gases, radiant burners, catalyst supports, biomedical devices, kiln furniture, bioreactors, supports for space mirrors, components of solid-oxide fuel cells, electrodes, heat exchangers, etc. [10].

As filters, porous ceramics can be used as size-selective filters to separate various species on the basis of the pore size of the ceramic. For example, a gas or a liquid may be passed through a porous ceramic, where larger particles may be retained, while smaller particles or species may pass through. Porous ceramics can also be used as a support for a catalyst or as an absorbent. As such they have a relatively open structure and a high surface area onto which the catalyst can be adsorbed.

1.3 Colloidal processing of ceramics

1.3.1 Some brief words on the nomenclature

The terms ‘‘agglomerate’’ and ‘‘aggregate’’ are widely used by powder technologists to describe assemblages of particles that are found in dry powders and powders in liquid suspensions. Each term has a specific meaning but, unfortunately, they are frequently interchanged, and this has resulted in an almost universal confusion. This confusion is perpetuated by conflicting definitions in national and international standards and this presents problems when describing powder properties or communicating results in reports and research papers[11]. The authors suggest that a single term that is universally understood and accepted to describe an assemblage of powder particles is needed. They propose that when particle assemblages are described, the term agglomerate is used exclusively. Where specifically required, hard and soft agglomerates can be distinguished, with brittle agglomerates being used to describe hard agglomerates that can only be fractured by applying considerable force. The term aggregate should be confined to pre-nucleation structures that arise from the association of molecules into supra-molecular structures, which in turn may develop into agglomerates.

1.3.2 Experimental research

In recent years, considerable effort was directed to the design and fabrication of nanostructured materials. The increasing interest in nanomaterials is attributed to their unique properties, which are a function of their size, composition and structural order. Among them, the electrical and mechanical properties are attracting special attention. It is believed that a nanostructured material should exhibit higher flexural strength values when either biscuit or densely sintered. Because of these specific properties, effective strategies of designing tailored bulk nanomaterial, which can be shaped predictably and reliably, are underway. The most straightforward approach includes the drying of synthesized nanopowders, but this inevitably results in their agglomeration. Therefore, a colloidal approach to the preparation of bulk ceramic pieces is attractive in order to create ordered and complex materials. Since it is almost impossible to wet-shape mono-disperse nanoparticles, research has been focused on the preparation of core-shell colloidal materials with tailored structural, optical, and surface properties[12].

PARTICLE ENGINEERING[13] is the term used to describe the synthesis of core-shell particles with defined morphologies and properties. Caruso, in his review article, provides an overview of the various methods used to synthesize core-shell particles in the nanometer to the micrometer size range. They are divided into three main groups with subgroups:

1. Polymer coatings:
    - surface modification via polymerization processes
    - self-assembled polymer layers
2. Bio-macromolecular layers
3. Inorganic and composite coatings:
    - precipitation and surface reactions
    - controlled assembly of preformed nanoparticles

A number of polymerization-based methods have been used to obtain particles of solid cores coated with a shell of polymeric materials. These include monomer adsorption onto the particles' surface followed by polymerization, named hetero-agglomeration–polymerization, and emulsion polymerization in which core particles are encapsulated by polymer layers. The layer-by-layer (LbL) colloid templating strategy falls into the self-assembled polymer layers group, where polymers are adsorbed onto the particle`s surface due to differences in the surface charge between the two. Using this strategy a shell constructed of a multilayer of polymers can be attached to the core particle surface, as shown in Figure 1.

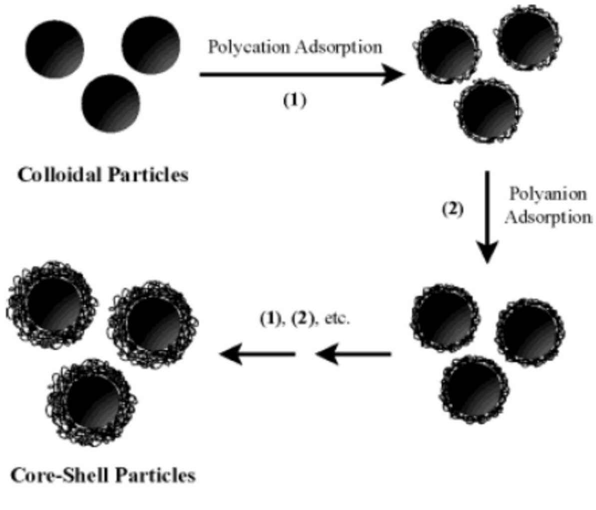

Figure 1: Schematic illustration of the LbL process for forming polyelectrolyte multilayers on particles. The scheme is shown for negatively charged particles. The process involves the sequential deposition of oppositely charged polyelectrolytes onto colloidal particles, exploiting primarily electrostatic interactions for a polymer multilayer build-up. Following the deposition of each polymer layer, any excess polyelectrolyte is removed by centrifugation

or filtration, with intermediate washings with water. The key to the formation of the polyelectrolyte multilayers is that not all of the cationic (or anionic) groups of the deposited polyelectrolyte interact with the particle surface (or the underlying polymer layer beneath). Hence, non-utilized charged groups, which cause charge overcompensation, facilitate the electrostatic binding of the subsequently adsorbed layer. Finally, a polyelectrolyte multilayer film of tailored thickness is obtained on the colloidal template via this strategy.

Because of the importance of proteins in biotechnology, bio-macromolecular layers include immobilized proteins on solid supports, whereas various procedures were employed to fabricate inorganic and hybrid coatings on particles. The precipitation can be performed either by direct surface reactions with the core particle`s surface or by surface reactions utilizing specific functional groups to induce the coating of the core particles.

Yet another approach includes the controlled assembly of preformed nanoparticles where electrostatic interactions are exploited to prepare core-shell materials, as schematically shown in the work of Wu et al[14] (Figure 2).

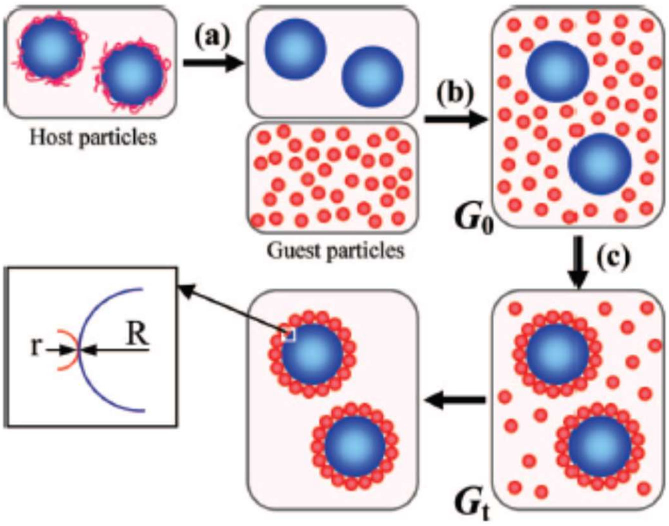

Figure 2: Schematic representation of the proposed hetero-coagulation strategy by Wu et al.

To begin with, each colloidal particle exhibits a surface charge when immersed in a polar medium, e.g., water. The area of particle engineering offers an agglomeration method, i.e., hetero- or homo-agglomeration that can occur between particles with a different size, shape, sign of surface charge and surface charge density. It is an effective tool for designing core-shell nanocomposites with tailored morphologies. Employing the agglomeration approach, a homogeneous distribution of shell particles attached to the surface of core particles can be achieved[15,16].

The theoretical background for the latter strategy is taken from the DLVO theory. This theory is well recognized in the field of inter-particle interactions but some basic points will be explained in one of the following chapters.

1.3.3 Theory of inter-particle interactions

1.3.3.1 Origin of the electrical double layer and zeta-potential

The stability of colloidal particles in polar liquids, i.e., water, is ensured by the formation of the double layer of ions that arises near the colloid particle surface in order to neutralize its surface charge[17]. The surface charge of ceramic particles is a consequence of the formation of a metal-hydroxide (MeOH) when a ceramic particle is in a polar medium. At acidic pH values the hydroxide protonates, gaining a positive surface charge, and at higher pH values it de-protonates, gaining a negative surface charge[18]. The sequence is presented here:

$$\mathrm{MeOH_2^+} \xleftarrow{H^+} \mathrm{MeOH} \xrightarrow{OH^-} \mathrm{MeO^-} + \mathrm{H_2O}$$

Each ceramic material at certain pH value contains the same net amount of positive and negative sites on its surface and therefore its net surface charge is zero. This point is termed the point of zero charge (PZC).

The obtained surface charge is neutralized by ions that are present in the liquid medium. The double layers consist of the Stern and diffuse layers. They are divided by the shear plane, commonly denoted as the slip plane or the zeta plane. The former may be thought of as being rather immobile in the sense of mobility normal to the surface since, if the adsorption forces are strong, the life time of an ion in the layer will be rather long. There is also the question of lateral mobility, or resistance to shear. It seems likely that the ions and surrounding medium in the Stern layer would be rather rigidly held and that the Stern layer itself would also be immobile in the sense of resisting shear. Since this type of immobility refers to the medium as a whole, and hence primarily to the solvent, there is no reason why the shear plane should coincide exactly with the Stern layer boundary and, as suggested in Figure 3, it may well be located somewhere further out. The potential at the shear layer is known as the zeta-potential and it can be regarded as the potential difference in an otherwise practically uniform medium between a point some distance from the surface and a point on the plane of the shear. The zeta-potential is not strictly a phase-boundary potential because it is developed wholly within the fluid region. It is of the order of millivolts[19]. The point where the zeta-potential reaches a value of 0 mV is defined as the isoelectric point (IEP).

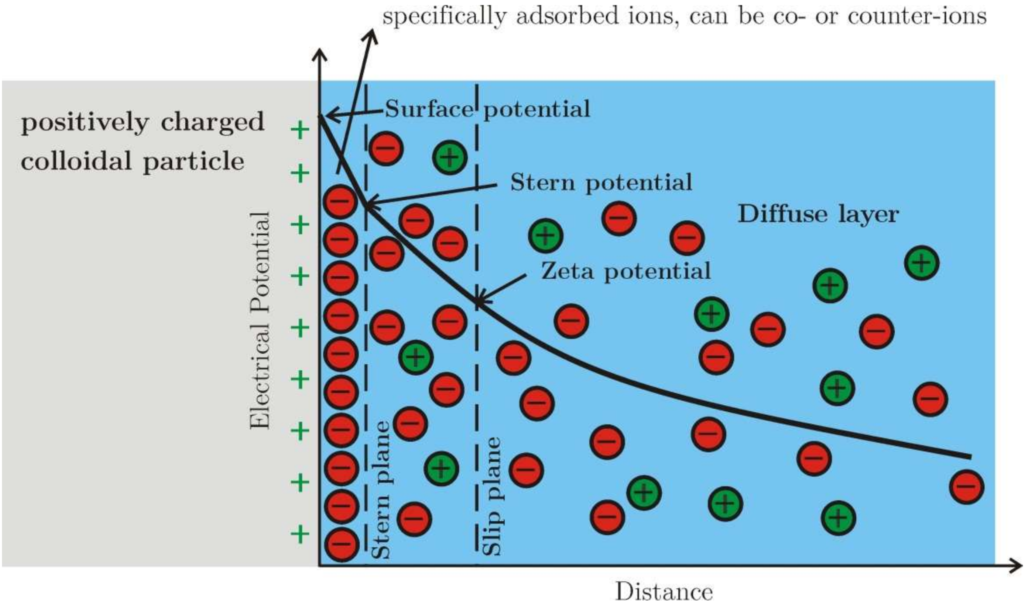

Figure 3: Schematic representation of the potential decay away from the surface.

1.3.3.2 The DLVO theory explains the tendency of colloids to agglomerate or remain discrete

The DLVO Theory (named after Derjaguin, Landau, Verwey and Overbeek) is the classic explanation of the stability of colloids in a suspension. It looks at the balance between two opposing forces — the electrostatic repulsion and the van der Waals attraction — to explain why some colloidal systems agglomerate while others do not[20,21].

The situations in which van der Waals forces alone determine the total interaction are restricted to a few simple systems, for example, to interactions in a vacuum or to non-polar wetting films on surfaces. In more complex systems, long-range electrostatic forces are also involved, and the interplay between these two interactions has many important consequences.

Unlike the double-layer interaction, the van der Waals interaction potential is largely insensitive to variations in the ion electrolyte concentration and the pH, and so may be considered as fixed in a first approximation. Furthermore, the van der Waals attraction must always exceed the double-layer repulsion at small enough distances since it is a power-law interaction (i.e., $W \propto -1/D^n$), whereas the double-layer interaction energy remains finite or increases much more slowly as D → 0. Figure 4 shows schematically the various types of interaction potentials that can occur between two surfaces or colloidal particles under the combined action of these two forces.

Depending on the electrolyte concentration and the surface charge density or potential, one of the following may occur:

1. For highly charged surfaces in a dilute electrolyte, there is a strong long-range repulsion that peaks at some distance, usually between 1 and 4 nm, at the *energy barrier*. This is illustrated in Figure 4 with curve a.

2. In more concentrated electrolyte solutions there is a significant *secondary minimum*, usually beyond 3 nm, before the energy barrier. The potential energy minimum at the contact is known as the *primary minimum*. For a colloidal system, even though the thermodynamically equilibrium state may be with the particles in a contact in the deep primary minimum, the energy barrier may be too high for the particles to overcome during any reasonable time period. When this happens, the particles will either sit in the weaker secondary minimum or remain totally dispersed in the solution. In the latter case the colloid is referred to as being *kinetically stable* as opposed to *thermodynamically stable* (Figure 4 - curve b).
3. For surfaces of low charge density or potential, the energy barrier will always be much lower (Figure 4 - curve c). This leads to slow agglomeration. Above some concentration of electrolyte, known as the *critical coagulation concentration*, the energy barrier falls below the $W = 0$ axis (Figure 4 - curve d) and the particles then agglomerate rapidly. The colloid is now referred to as being unstable.
4. As the surface charge or potential approaches zero the interaction curve approaches the pure van der Waals curve, and the two surfaces now attract each other strongly at all separations (Figure 4 - curve e).

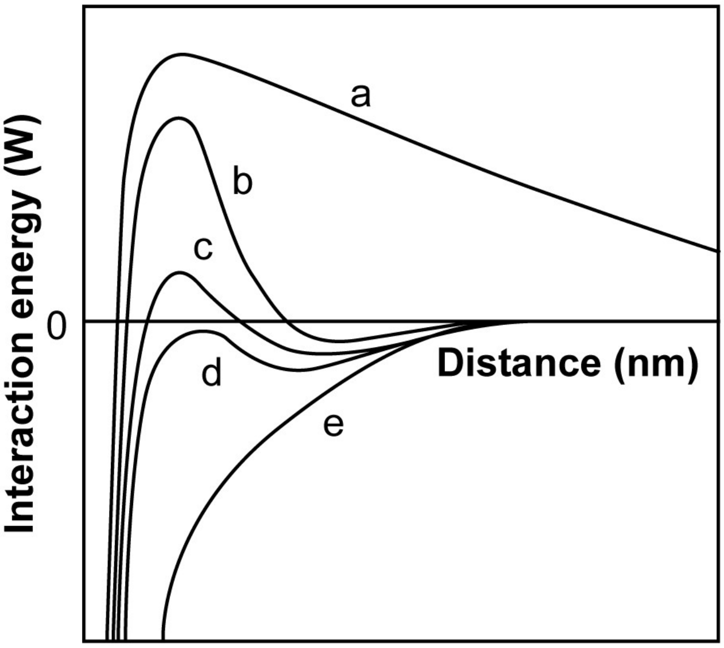

Figure 4: Schematic energy versus distance profiles for a DLVO interaction. (a) Surfaces repel strongly; small colloidal particles remains “stable”. (b) Surfaces come into stable equilibrium at a secondary minimum if it is deep enough; colloids remain “kinetically” stable. (c) Surfaces come into secondary minimum; colloids coagulate slowly. (d) The “critical coagulation concentration”. Surfaces may remain in secondary minimum or adhere; colloids coagulate rapidly. (e) Surfaces attract each other and colloids coalescence rapidly.

1.3.3.3 The extension of the DLVO theory by Hogg, Healy and Furstenau

Hogg, Healy and Furstenau extended the DLVO theory to include the interaction between spherical colloidal particles of different radii, R and r, and different surface potentials[22,23]. The interfacial potential V_{TOT} between the two particles, differing in the above parameters, in the suspension can be calculated using equations 1 and 5. Equations 1 to 4 describe the electrical double layer interaction (V_{DL}) for two spherical particles denoted as the core (c) and shell (s) particles:

$$V_{DL}=\left(\frac{\varepsilon_r}{4}\right)g_{cs}(\psi_c^2+\psi_s^2)\left\{\left(\frac{2S}{1+S^2}\right)ln\left[\frac{1+exp(-\kappa D_0)}{1-exp(-\kappa D_0)}\right]+ln[1-exp(-2\kappa D_0)]\right\} \qquad (1)$$

here $\varepsilon_r = 4\pi\varepsilon\varepsilon_0$, ($\varepsilon_0 = 8.85 \cdot 10^{-12}$ As/Vm), where ε_0 is the permittivity of the vacuum, ε is the dielectric constant of the medium. ψ_c and ψ_s are the surface potentials of the core and shell particles, respectively, and D_0 is the distance between the interacting particles. A measure of the double-layer thickness is the Debye length κ^{-1} and is given by equation (2):

$$\kappa^{-1}=\left(\frac{\varepsilon\varepsilon_0 kT}{e^2\sum n_i z_i^2}\right)^{1/2} \qquad (2)$$

where k is the Boltzmann constant, T is the temperature, e is the electronic charge, n_i is the number concentration of the ion i in the medium and z_i is the valence of the ion i.

Factor g_{cs} depends upon the radii of the particles and is given by eq. 3:

$$g_{cs}=(R_c^{-1}+r_s^{-1})^{-1} \qquad (3)$$

where R_c and r_s are the radii of the core and shell particles, respectively.

The surface potential ratio S is defined by eq. 4:

$$S=\frac{\psi_s}{\psi_c} \qquad (4)$$

The total interaction between any two particles must also include the van der Waals attraction and eq. 6 estimates the London–van der Waals attractive interaction V_A as:

$$V_A=-\frac{A^*}{12}\left[\frac{y}{x^2+xy+x}+\frac{y}{x^2+xy+x+y}+2ln\left(\frac{x^2+xy+x}{x^2+xy+x+y}\right)\right] \qquad (5)$$

where A^* is the Hamaker constant of the interacting particles[24]; and x and y represent the $D_0/2R_c$ and r_s/R_c ratios, respectively.

Because of the tightly adsorbed layer of counter-ions in the Stern plane, it is impossible to determine the values of the true surface potentials. Instead, the measured zeta-potential on the slip plane can be used. According to Bleier et al[23] the zeta-potential is preferred since the capacitance of the medium near the oxide surface cannot be measured. Consequently, the above equations are usually modified such that the zeta-potential and the zeta-potential ratio (ζ_S) replace ψ and S, respectively.

Recently, it has been shown by several authors that it is possible to use a Monte-Carlo simulation to estimate the effect of the particle size and the sign of charge on the course of the agglomeration when mixing two or more distinct particle species[25,26]. The authors showed that by designing the interactions in the suspension it is possible to influence the course of the solid-state reactions which enables the production of higher-quality materials. Furthermore, computer simulations help to understand what is happening at the particle level in the slurries and gives the possibility to further improve the experimental parameters.

1.4 Shaping of green bodies

1.4.1 Shaping of micron-sized particles

The purpose of modern ceramic processing is to better control the particle packing during consolidation and the microstructure during sintering, so that the shaped green samples contain fewer strength-determining flaws and after sintering fewer strength-degrading pores. In order to achieve such a goal, the selection of a proper shaping technique is of utmost importance. Shape forming can be carried out either by dry pressing or by one of the wet-forming techniques, i.e., slip casting, pressure filtration, etc. The reliability of engineering components shaped by dry pressing suffers from the detrimental heterogeneities that are already present in the granulated powder and are retained during the shape forming and densification.[27] They concentrate any applied stress to severely degrade the component's strength. Somewhat improved mechanical properties can be achieved with wet-forming methods that use slurries (particle/liquid mixtures), with which the strength-degrading agglomeration can be avoided. Furthermore, the uniformity of the colloidal state is reflected in the uniformity of the consolidated ceramic body[27,28,29]. Examples include tape casting[30] to form thin sheets (evaporation), slip casting[30,31] to form thin-walled bodies (capillary suction into porous mold), and pressure filtration[32,33,34]. Using these methods green bodies with a very high relative density of powder are formed. However, the liquid must flow through the consolidating body, which is time consuming, and the former two are limited to thin coatings or thin-walled pieces. Direct shaping methods start with slurries containing a high volume fraction of powder that can be either poured or injected into an impermeable mold. These methods are: injection molding (IM), gel casting (GC), direct coagulation casting (DCC) and hydrolysis-assisted solidification (HAS)[35]. In the case of IM and GC the liquid phase solidifies with either freezing or polymerization. For DCC the highly repulsive potential is converted to highly attractive and a strong particle network forms the engineering part. During HAS, AlN powder hydrolyses at elevated temperatures, which results in the formation of boehmite lamellas that connect the powder particles into a solid body.

1.4.2 Shaping of nanoparticles

The interest in ceramic nanoparticles and their processing into nanomaterials and nanocomposites has led to their extensive study. Nanopowders are expected to produce promising materials in terms of strength, hardness and wear[36]; however, the traditional "know-how" about suspensions cannot just be transferred and applied from the case of micron- and submicron-sized particles. There are numerous parameters and interactions to control. In order to achieve satisfactory green densities a high solids loading of the suspension must be assured, otherwise cracks will form during the drying and sintering. The dispersion of nanosized ceramic particles at high solid loadings in a slurry is still a challenge. However, there are dispersants that give sufficient dispersive forces in order to overcome the attractive van der Walls forces. The best results could be obtained if the dispersive forces are over a very short range, so that the particles can be packed as densely as possible and consequently a high solids loading of the suspensions can be achieved. It is therefore of crucial importance to select the right dispersion mechanism (electrostatic, steric, electrosteric) and, consequently, the appropriate dispersants and the dispersion medium.

The stabilizing mechanisms are based on a charge, a surfactant layer or both to form a barrier and hinder agglomeration. These barriers increase the hydrodynamic volume of the dispersed particles, and consequently the effective solid volume fraction $\O_{\mathrm{eff}}$ remains constant, but the maximum filling level $\O_{\mathrm{m}}$ is decreased (Figure 5). In the case of mono-dispersed spherical particles this can be defined as:

$$\emptyset_{eff} = \emptyset(1+\frac{\Delta}{r})^3 \tag{6}$$

where r is the radius of particles, Δ is the thickness of the repulsive barrier; $\O_{\mathrm{eff}}$ and Ø are the effective volume fraction and the volume fraction of the solid phase, respectively[37].

It is thus important to form a barrier that is sufficient to act as a dispersant but still allowing high packing of the particles to be attained. The barrier increases the particle radius to an effective radius r + Δ. It is obvious that the packing density decreases with a decreasing particle size and this is especially true in the nanosize range (10-100nm). So with the use of a 20-nm-thick coating a packing density of less than 0.5 is achieved when the particle size is 0.5 µm. If the layer thickness is decreased to 5 nm the packing density is increased to 0.6, again at a particle size of 0.5 µm. It is assumed that for micron-sized particles the thickness of the adsorbed layer can be neglected, because of the small ratio Δ/r. The solids loading of the suspensions in this case are not affected and have for spherical particles a value of ≈ 64%[38]. If the particle size is reduced to 10 nm the same thickness of the coating significantly affects the packing density and at colloid volume fraction of 0.1, the effective volume fraction becomes 0.45.

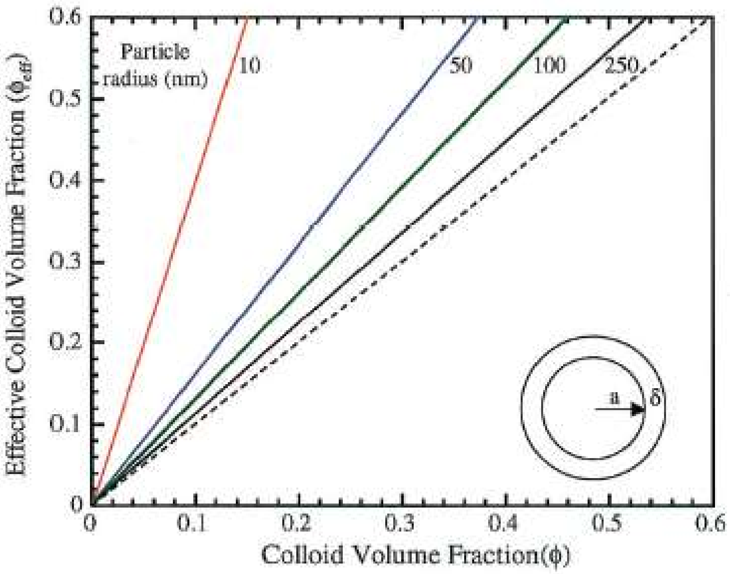

Figure 5: Effective colloid volume fraction as a function of the actual colloid volume in a slurry. Colloids of varying sizes and constant adlayer (10nm) thicknesses are shown.

Due to above reasons, it is at present impossible to prepare nanoparticle suspensions with sufficiently high solid loadings to be used in existing wet-shaping methods[37,39]. On the other hand, if nanoparticles are spray dried to obtain a granulate the resulting granules are not weak enough to be crushed during dry-pressing, even when using pressures as high as 380 MPa. Therefore, nanoparticles processed in this way lose their expected character[40]. Raghupathy et al[40] introduced the method of spray freeze drying, with which they claim that crushable granules are produced and a nanostructure is obtained in dry-pressed green samples. However, during processing the authors observed a lower fill density, which concurrently with a consideration of the colloidal processing during the preparation of the starting suspension, indicates the presence of agglomerates and the conclusions need to be looked at again.

1.5 Microstructure evolution during sintering

Sintering refers to the process of firing and densification of a body shaped from powder particles[41]. It is a process during which a porous material with a high specific surface area is expected to consolidate at high temperatures into a solid product with minimized surface area. The temperature of the sintering is lower than the melting temperature and as a consequence the final product retains the shape of the green body that is formed from uni-axial pressing or cold-isostatic pressing, slip casting, injection moulding, pressure filtration, etc[42]. In the strict sense of the word sintering denotes the process in which the fine particles of a material become chemically bonded at a temperature that is sufficient for atomic diffusion.

1.5.1 Stages of sintering

The sintering process is commonly divided into three stages (Figure 6). In the initial (1st) stage the network of particles starts to form and it is marked by neck formation[43]. The individual powder particles are still distinguishable. In this stage, as is shown in Figure 7a, the relative density of the material increases by roughly 3%. Most of the densification as well as the greatest microstructural change occurs in what is termed the intermediate stage (2nd stage), where voids form continuous pore channels along three-grain junctions (Figure 7b). The pore channels are formed when the individual powder grains become well bonded during the initial stage. With time the pore channels tend to shrink due to the diffusion of the atomic vacancies away from them; however, the grain growth occurring at the same time leads to a reduction in the total number of pores and tends to increase their average diameter and length as a consequence of coalescence. The process continues until the network of pores undergoes the so-called Rayleigh breakup,[44] first into progressively fewer interconnected elongated pores on the grain edges and finally into isolated pores at the grain corners, at which point the final stage of sintering begins. When the density of a material exceeds 90–94% of TD the isolated pores are formed and the densification is slowed down. In the 3rd or final stage of sintering these isolated pores are eliminated by the transport of mass from the grain boundary to the pore. The densification is pinned by pores and a lot of energy is necessary for further densification. In this stage the grain growth dominates the sintering process.

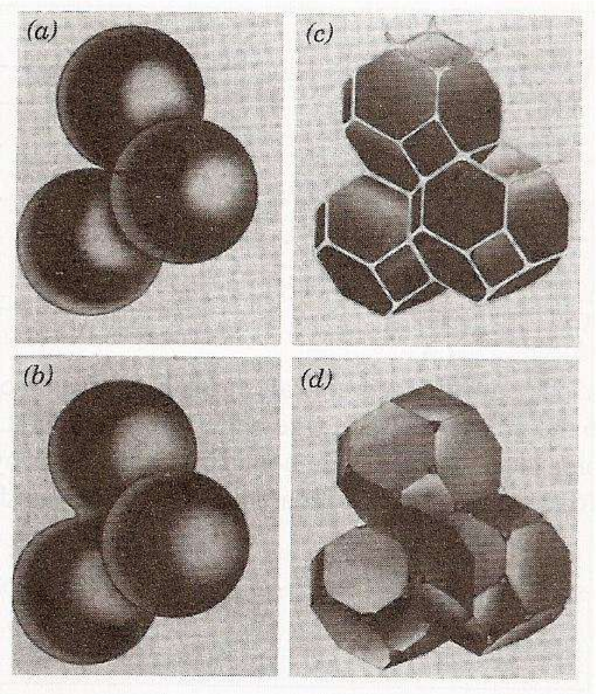

Figure 6: Stages of sintering: (a) Initial stage; model structure presented by spheres in tangential contact. (b) Near end of initial stage. Spheres have begun to coalesce. (c) Intermediate stage: dark grains have adopted shape of tetrakaidecahedron, enclosing white pore channels at grain edges. (d) Final stage: pores are tetrahedral inclusions at corners where four tetrakaidecahedra meet[45].

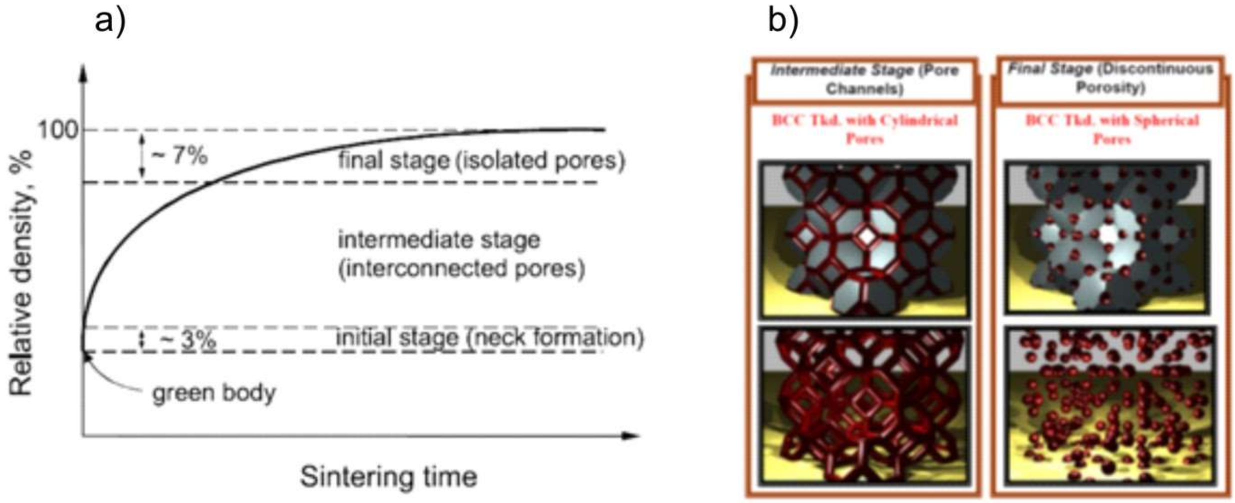

Figure 7: Stages of sintering showing in a) the densification curve and in b) the phenomenological model for the intermediate and final stage of sintering. Pictures in the above show the packing of spheres and those below show the porous structure of porosity[46].

1.5.2 Driving force for sintering, i.e., sintering stress

The system of powders has a higher free energy compared to the same volume of a compacted body. This is a consequence of a higher specific surface area and the disordered crystal structure on the surface of the individual particles of a powder. During sintering a drop in the free energy is observed. This is a consequence of shrinkage, the lowering of internal stresses, the lowering of the concentration of irregularities in the crystal lattice and reducing the free surface area. The process of sintering can therefore be described as a thermodynamic process in which the system tends to occupy the state with the minimum free energy[47,48,49]. The sintering of crystalline materials is complex. The driving force is the minimization of the surface energy, which is for crystalline substances mostly higher than for amorphous solids. A specific interfacial energy arises where the two individual particles meet and the area is called a grain boundary. It is said that some of the energy gained by eliminating the solid-gas interface is used to create a longer grain boundary. There are number of competing paths for material transport to the neck area during sintering[49,50]. Whether the sample will densify or not depends entirely on which transport mechanism will dominate during the sintering. The two possible mechanisms for neck growth without densification are evaporation-condensation and surface diffusion. As shown in Figure 8 these move the material from the particle surface to the neck and so reduce the surface energy. However, neither of them causes densification, since no mass is removed from the inter-particle junction or the grain boundary.

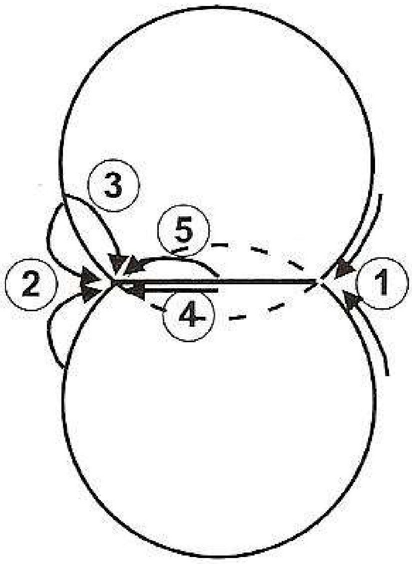

Figure 8: Sintering at the contact point between two crystalline particles. Pathways 1-3 surface diffusion, vapor phase transport and lattice diffusion from the particle bulk to the neck lead to coarsening, but not to shrinkage. Pathways 4 and 5, grain-boundary diffusion and lattice diffusion from the grain boundary to the neck lead to shrinkage. (Brinker, Scherer, Sol-Gel science, Academic press, Boston 1990).

Densification mechanisms are those in which the grain-boundary plane serves as the source of diffusion transport and the neck as the repository for atoms. These processes take place either along the grain boundary or through the lattice (Figure 8). In both cases the driving force for the diffusion is the gradient in stress between the surface of the neck and the grain-boundary plane. The net curvature of the neck causes a tensile pressure of:

$$\Delta p = \gamma\left(-\frac{1}{\rho} + \frac{1}{x}\right) \tag{7}$$

where x is the radius of the neck and ρ is the negative radius of neck curvature. Because x has a much higher value than ρ the equation can be written as

$$\Delta \mathrm{p} = -\frac{\gamma}{\rho} \tag{8}$$

The negative sign indicates that there is a tensile stress and the neck is trying to level up.

One consequence of the pressure difference across a curved surface is the difference in chemical potential between the surfaces with different radii of curvature. The pressure applied to the liquid or solid by the curved surface increases the chemical potential of its constituents and in this the vapor pressure at equilibrium. A convex surface has a greater equilibrium vapor pressure than a planar surface, which has a greater vapor pressure than the concave surface.

The difference in chemical potential is written as:

$$\Delta\mu = \Delta p \Omega \quad (9)$$

where Ω represents the atomic volume.

From equations 8 and 9 the difference between the potential of a plane and curved surface is written as:

$$\mu - \mu_0 = -\frac{\gamma\Omega}{\rho} \quad (10)$$

If the chemical potential is expressed with the Kelvin equation, which is $\mu = RT(\ln p/p_0)$, then

$$RT \ln\left(\frac{p}{p_0}\right) = -\frac{\gamma\Omega}{\rho} \quad (11)$$

here p_0 and p are vapor pressures over the plane surface and curved surface, respectively. Eq. 11 expresses the fact that material will evaporate from a plane surface and will be deposited on a curved surface. The effect of the particle diameter in these relations is an important reason for using fine particle-size materials. It is common in ceramic processing to synthesize powders of submicron particle size, which as a consequence induce higher capillary forces.

The diffusivity of atoms in a substance during sintering has its foundations in the crystal defects (vacancies) present in a solid (Figure 9). The concentration of vacancies depends on the temperature and chemical potential under the surface. If the Kelvin equation is used again thn:

$$\mu - \mu_0 = -\frac{\gamma\Omega}{\rho} = \mathrm{RT}\ln\left(\frac{\mathrm{c}}{\mathrm{c}_0}\right) \quad (12)$$

where c and c_0 mark the concentrations of vacancies under the curved and plane surfaces, respectively.

It is known that there is a higher concentration of vacancies under a curved than under a plane surface, which induces the flow of atoms from plane to curved surfaces. If a diffusion coefficient is used, the current of atoms is written with the equation:

$$J = -D_v \Delta c / \Delta x \quad (13)$$

and

$$D_v = Dc_0 \quad (14)$$

here D denotes the diffusion coefficient of atoms and D_v the diffusion coefficient of vacancies, Δc is the concentration difference of vacancies and Δx is the increase in the radius of the neck.

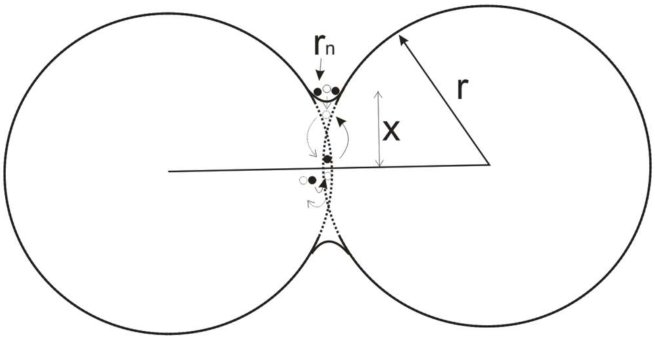

Figure 9: Migration of vacancies to the grain boundary and their recombination. The black circles present the atoms and the empty circles represent the vacancies.

The neck can grow because of the diffusion of atoms from the area of the plane to the area of the curved surfaces and in this way the radius of curvature is reduced. This process in turn equalizes the difference in the concentrations of vacancies under the aforementioned surfaces.

The activation energies for the diffusion processes increase typically in this order: surface diffusion < boundary diffusion < lattice diffusion. This fact explains that at low temperatures it is predominantly grain growth without shrinkage that occurs, while at higher temperatures it is boundary and lattice diffusion that will govern the sintering process. Shrinkage and loss of pore volume will occur in the latter case.

It should be noted at this point that the activation energy for material-transport mechanisms also depends on the size of the powder particles. This was shown by Theunissen et al,[51] who studied the sintering kinetics. Since isothermal sintering experiments present several problems, the most important of which is the inability to study the initial portion of the sintering process, non-isothermal treatment or constant-rate-of-heating (CRH) experiments were chosen in their study. The CRH treatment also enables the separation of sintering mechanisms with different activation energies, whereas these mechanisms may overlap using isothermal conditions[52]. The result of the studies was that nanoparticles exhibit lower activation energies than micron-sized particles do and therefore initiate the sintering process at lower temperatures.

Eq. 12 indicates that for the diffusion of atoms, empty neighboring spaces, i.e., vacancies, are needed. The concentration of vacancies strongly depends on the temperature and on the concentration of impurities. If matter is expected to rearrange, as is the case in sintering, the activation energy must be overcome (Figure 10).

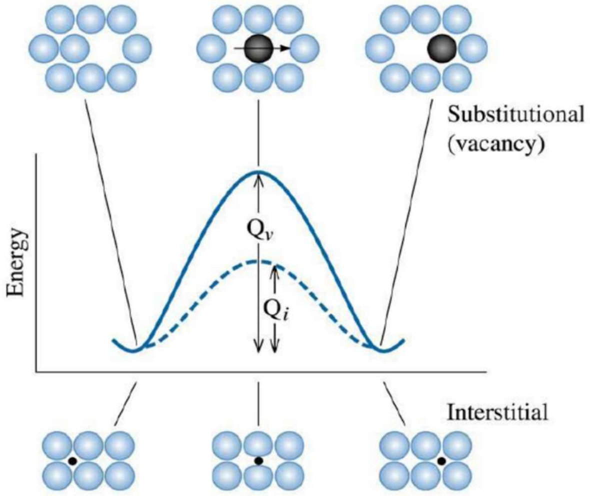

Figure 10: Diffusion of a single atom. In order for the atom to diffuse from one state to the other the energy-barrier activation energy Q must be overcome.

1.5.3 Sintering of nanoparticles

The sintering of nanoparticles presents additional challenges to those of sintering regular powders. These challenges arise from their agglomeration during processing, high reactivity and inherent contamination, marked grain coarsening and as a result of this to the ultimate loss of the nano-features. These drawbacks will be resolved by improvements to nanopowder synthesis methods, improvements in shaping methods and by understanding the process of their densification[53]. According to several authors, it is important to resolve the question of whether the sintering of nanocrystalline materials involves the same mechanisms as those of conventional materials[54,55].

Nanopowders are thermodynamically unstable because of their large surface area. They have different surface energies due to different local atomic arrangements at the surface. The sintering of nanopowders is kinetically enhanced, thus lowering the sintering temperatures to 0.2-0.3 of the melting temperature (T_m), as compared to conventional powders that sinter at 0.5-0.8 T_m. Surface diffusion is expected to be rapid in the early stages of sintering. Molecular-dynamics simulations indicated the extremely fast sintering of nanoparticles, in fact so fast that the surface diffusion alone could not explain the phenomenon. In accordance with the experimental data some additional mechanisms are suggested:

1. grain rotation
2. grain-boundary slip
3. dislocation motion

Before the neck is formed adjacent particles rotate in order to minimize the grain-boundary energy and the phenomenon was confirmed with TEM studies[56,57]. In nanomaterials the sub-grain coalescence has also been observed, which must involve lattice rotation and is important only at the small grain size where the kinetics of rotation are more rapid. The coalescence of the sub-grain lattice may have some importance in the nucleation of re-crystallization or grain growth. This sub-grain coalescence can be described with two mechanisms as the reduction of strain energy by moving dislocations from widely-spaced arrays to a finer one or the sequential removal of dislocations from small-angle boundaries in response to unbalanced forces at the ends of a dislocation array[58,59,60].

1.5.4 Sintering of granulated ceramic powders

If granulated (agglomerated) ceramic oxide powders are shaped into green compacts by dry pressing, green bodies with two types of pores are obtained, namely inter-agglomerate pores, which are measured in microns, and inter-crystallite pores, measured in nanometers (Figure 11). During sintering higher temperatures are needed for the elimination of inter-agglomerate pores, which consequently lead to grain growth. This is in conflict with the aim of keeping the sintered grain in the nanometer regime. Most often the pore distribution is dictated by the value of the green density. In non- or weakly agglomerated powders a high green density with a small pore population is easily reached. Open pores in nanopowder compacts inhibit grain growth in a similar way that pores prevent grain coarsening in conventional grained ceramics[61].

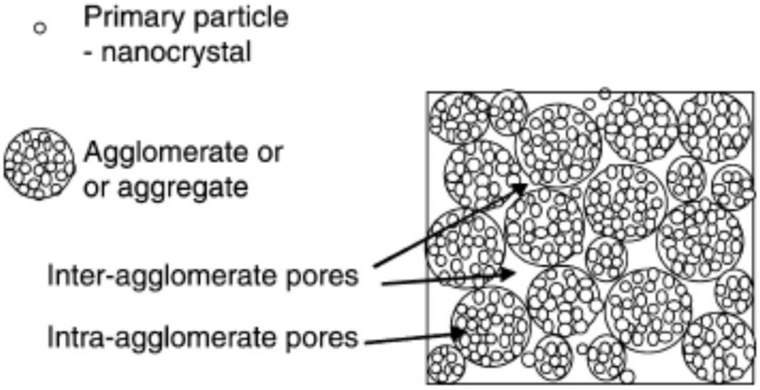

Figure 11: Schematic illustration of primary particles (nanocrystallites), an agglomerate and the packing of agglomerates.

1.5.5 Sintering of bimodal particle mixtures

The mixing of coarse and relatively fine ceramic powders has been used to control firing shrinkage for a very long time[62]. It is well known that mixtures of this type can increase the green density, although the increase is often less than the theoretical prediction[63]. The consequence of mixing in ceramic materials is a pronounced change in their sintering kinetics. As reported in the literature for a heterogeneously distributed bimodal mixture, the addition of fine particles in volume fractions greater than 30 vol. % controls and enhances the densification, whereas at lesser volume fractions of fine particles the coarser fraction dominates over the densification process[64]. The effect of the particle size distribution on the sintering of ceramics depends on how the particle size distribution is changed during the processing. Some studies have examined the effect of changing the standard deviation of the particle size distribution while keeping the median particle size constant. It has been found that wider particle size distributions lead to faster densification rates in intermediate stage sintering[65]. However, a narrower distribution may prolong intermediate stage sintering and result in less coarsening in the final stage[66]. For bimodal distributions of alumina powder mixtures it was observed that the densification rate is retarded compared to monomodal packing[67]. Another report by Wonisch et al., based on a discrete-element microscopic simulation, states that an overall decrease in densification should be expected when the width of the particle size distribution is increased[68].

1.6 The role of porosity in the flexural strength and elastic modulus

Another definition of sintering states that it is a heat-treatment process aimed at transforming a powder compact of limited cohesion into an engineering component of considerable strength[69]. This transformation is always a consequence of geometric changes to the internal geometry of a solid and of a pore space. Understanding the changes in microstructure is essential for controlling the densification and the mechanical properties. Coarsening of the pore structure as a consequence of particle rearrangement is an experimental fact and should be considered in the sintering and mechanical properties[70].

In order to increase the strength and reliability of the ceramics, it is necessary to understand how the strength evolves during fabrication. Packing errors in powder processing will have a tendency to persist throughout the sintering process. The packing of particles is rarely perfect and it presents the biggest problem with fine particles. The bridging of agglomerates leads to large void spaces after shaping and these have a tendency to grow during sintering. The fate of the porosity depends on the thermodynamics and can result in differential sintering, i.e., where different parts of a sample shrink at different rates. According to Kingery and Francois, pores with a concave surface curvature are thermodynamically unstable, shrink, and finally disappear if kinetically permitted[71]. Pores with a convex surface curvature, however, shrink to an equilibrium size, dependent on the grain size and the dihedral angle[72]. A dihedral angle and the number of grains surrounding the pore define the surface curvature of the internal pores that are located at the grain junctions.

The dihedral angle or the angle of etching is determined by the ratio of the grain-boundary energy to the surface-liquid or surface-vapor interface energy and it is given by:

$$\gamma ss = 2\gamma_{SV} cos\frac{\varphi}{2} \qquad (15)$$

$$\gamma ss = 2\gamma_{SL} cos\frac{\varphi}{2} \qquad (16)$$

where γ_{SS} denotes the interfacial energy solid-solid, γ_{SL} denotes interfacial energy solid-vapor, γ_{SL} denotes the solid-liquid interfacial energy and φ is the dihedral angle.

If a 2D perspective is used, a pore surrounded with six grains has flat surfaces and is stable; the dihedral angle has a value of 120°. In a 3D perspective and under the condition that the dihedral angle measures 120° twelve grains are needed around the pore, so that the pore is stable. As the dihedral angle varies through the specimen the pores tend to grow or shrink, depending on the number of surrounding grains (Figure 12 a, b).

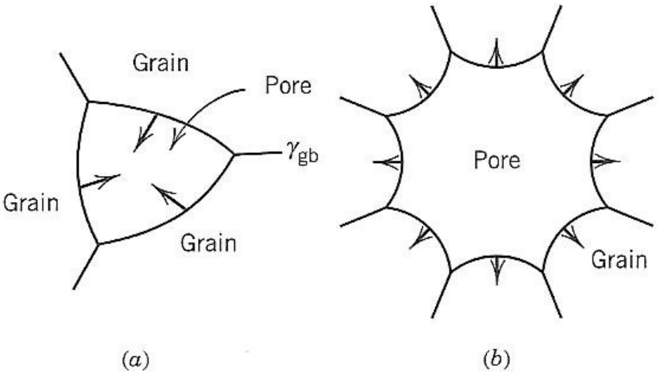

Figure 12: (a) Pores with few neighboring grains tend to shrink, while (b) pores with many sides tend to grow.

During previous decades, significant progress in the understanding of the physical background for this phenomenon has been made, but there are still open questions. A major problem in the field is the 3D interconnectedness of the porosity when attempting to assess its geometrical details experimentally or by theoretical and numerical modeling. Closed pores may form at density levels as low as 60-80% of the relative density, but a considerable part of the pore space is interconnected up to high relative densities, in excess of 80%[70]. In green powder compacts and during the initial stages of sintering a large number of irregular channels with a multitude of branches lead from larger open spaces to the sample surface. Consequently, the samples are permeable for liquids and gases. The length of the interconnected pore space is identical to the outside dimensions of the sintering part. Later on in the sintering process the pores close and finally disappear, if the compact is sintered to full density. This simple concept states that the dimensions of the pore space decrease throughout the sintering process. The question arises if and how the coarsening observed for planar sections is related to the coarsening of the 3D pore space. One study answering this question was made by Flinn et al., where artificial flaws shrank concurrently with the increasing relative density[73]. In this context, the mechanical properties of porous ceramics can be dictated by two parameters, i.e., the pore characteristics and the microstructure.

1.6.1 Empirical studies describing the flexural strength and elastic modulus of porous ceramics

Porous materials may be prepared by a variety of procedures, such as the replica technique, [74,75] the sacrificial template technique, [76,77] and direct foaming[78]. In general, however, porous materials prepared using these techniques exhibit poor mechanical properties compared to their densely sintered counterparts[79]. In most cases, better control of the pore geometry and an improvement of the mechanical properties of the dense matrix are important factors to improve the performance and reliability of porous materials. In order to do that the sintering of powder compacts to a fixed degree of densification[80,81] seems to be the most experimentally prospective. The flexural strength dependence on relative density was demonstrated by several authors, as shown in Figure 13. It can be seen that the flexural strength increases with the relative density in an almost linear fashion.

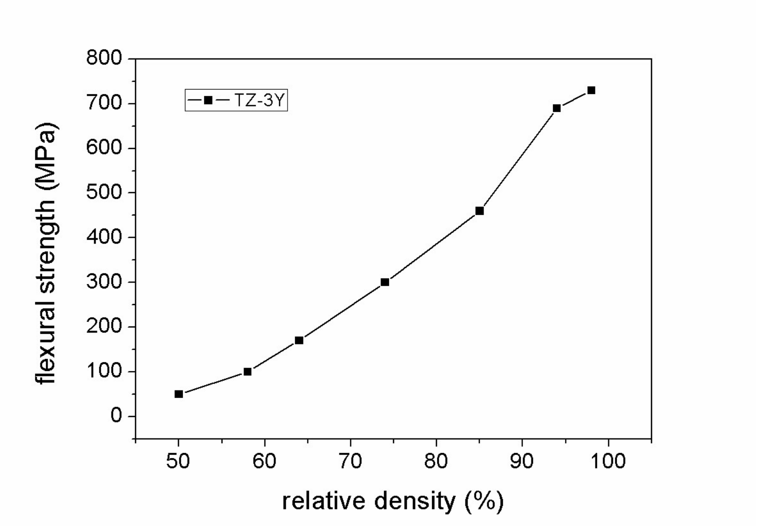

Figure 13: Flexural strength dependence on the relative density, adopted from Deng et al.[80]

As demonstrated by Hardy et al.,[82] surface diffusion results in the formation of necks between particles during the initial stage of sintering, which governs the mechanical properties of biscuit-sintered materials. Consequently, in order to increase the neck area of the dense matrix various approaches are being pursued, including the mixing of starting powders with different particle size distributions, i.e., a small addition of nanoparticles, resulting in an increased number of contacts,[83,84] the use of the dopants that enhance the surface diffusion of ceramic materials, which was extensively studied for dense ceramics[85,86] and not yet for porous ceramic materials. Yet another approach combines doping and the pulse electric sintering technique, which allows better control over the densification process[87]. Recently, another work was published stating that core-shell material exhibits a slower densification rate and also an increased flexural strength in the moderate porosity range compared to the biscuit-sintered core particles alone[88]. It was hypothesized that pore-space coarsening is responsible for the limited strength increase.

It has been well established in the literature that elastic modulus (E) exhibits a dependence on porosity contents in brittle solids and the relationship is given in equation 17 [89,90]:

$$E = E_0(1 - c_1P + c_2P^2) \quad (17)$$

where E and E_0 represent the elastic moduli of porous and dense materials, respectively, and P is the volume fraction of porosity, c_1 and c_2 are empirical constants that have been determined from experimental results by data fitting and have the values of 2,4 and 1,2, respectively. E dependence on relative density is shown in Figure 14.

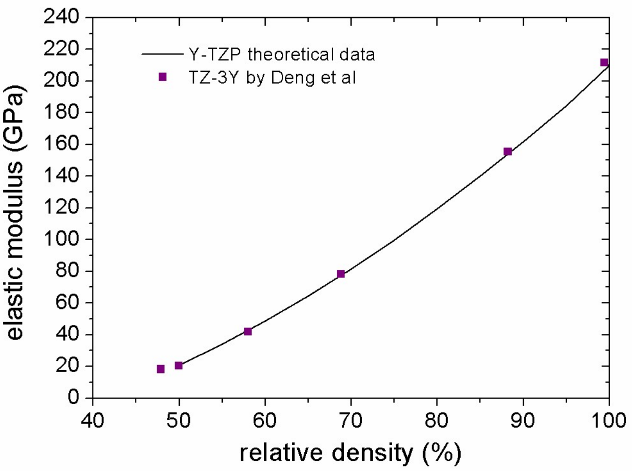

Figure 14: Elastic modulus dependence on relative density. Experimental results vs. theoretical calculations.

2 Aims and hypothesis

The purpose of this study was to develop moderately porous Y-TZP material exhibiting a high strength. One challenging solution to the problem seemed to be the introduction of nanoparticles. Their potential to display unusual physical and mechanical properties due to a high fraction of the atoms residing at the particle surface is very high. While commercial nanopowders have been produced successfully, a number of obstacles still need to be overcome if engineering parts are to be manufactured from them. First of all, there is an unresolved problem with achieving high green densities and, consequently, the prevention of crack formation during drying and/or sintering. The latter drawback is the reason why our work will involve the mixing of sub-micron-sized and nano-sized particles with an agglomeration method followed by slip casting. This is believed to be an effective tool for designing core-shell materials with tailored morphologies. The shaping of such a bimodal mixture is simpler than the shaping of just nanoparticles.

The porosity was intended to reduce the elastic modulus of Y-TZP ceramics, while retaining a useful flexural strength, so that the material can be used in dental applications. A reduced elastic mismatch between the dentine and the restorative Y-TZP material will be achieved, which may also result in a lower clinical failure rate. According to the literature[90], the elastic modulus of Y-TZP at the relative density of 70% has a value of 70 GPa. At this relative density the value of the flexural strength of dry-pressed and biscuit-sintered commercial material will be approximately 250 MPa, which is unacceptably low for dental applications. Our goal is to increase flexural strength to values exceeding 500 MPa, which is suitable for dental applications according to the ISO standard 13356:2008(E). It is expected that with the addition of nanoparticles to submicron-sized particles, moderately porous material exhibiting a sufficient flexural strength will be produced. Due to the larger area of the inter-particle contacts between the nano-sized and/or submicron-sized particles, the material will have a high enough strength so that it can be used in dental and other applications. In order to prevent any segregation during wet-shaping the agglomeration approach will be employed, enabling a homogeneous distribution of nanoparticles attached to the surface of the submicron-sized particles. The presence of nanoparticles will not only influence the area of the inter-particle contacts after biscuit-sintering, but will also prevent the evolution of strength-determining pores/flaws in a moderate porosity range.

3 Materials and Methods

3.1 Materials

To prepare a Y-TZP core-shell slurry using an agglomeration approach, zirconia core starting materials were prepared using a submicron-sized, granulated zirconia powder (TZ-3Y, Tosoh, Japan). Apart from the 3 mol % of Y_2O_3, which is present as an intentional zirconia tetragonal phase stabilizer, the main impurities measured in ppms are HfO_2, U_3O_8, ThO_2, Na_2O, CaO, SiO_2, Fe_2O_3 and Al_2O_3. The granule sizes vary from 10 µm to 80 µm and they are further composed of elemental crystallites that are less than 100 nm, which is in good agreement with the specific surface area (SSA) value, which is 16.4 m^2/g[91].

As a shell material, zirconia nanoparticles containing 3 mol % of Y_2O_3 and impurities such as SiO_2, TiO_2 and Fe_2O_3 in the ppm range, were used. The material is supplied in the form of an electrostatically stabilized aqueous suspension at pH 3.2–4.2 and a solids loading of 22–30 wt. %, depending on the batch received. The particle size is 11nm, as specified by the manufacturer (XZO1356/01, MEL chemicals, Manchester).

As a reference material the sub-micron-sized TZ-3YB powder, supplied as a ready-to-press granulate, was used. The material has similar characteristics to the TZ-3Y; the only notable difference is that it contains 3.7 % of binder.

Crystalline monohydrate of citric acid (Carlo Erba Reagents) was used to adjust the electrokinetic properties of the Y-TZP core material. All the slurries were prepared using deionized water.

The main characteristics of the as-received materials are listed in Table 1.

	Y_2O_3 mol%	BET, m^2/g	Particle size (nm)
TZ-3Y*	3	15.4	950
Nano Y-TZP*	3	/	11
TZ-3YB*	3	15.4	980

* Suppliers specifications

Table 1: The characteristics of the as-received materials.

3.2 Preparation of Y-TZP core particle suspension

The zirconia TZ-3Y core material was wet-attrition milled for 3h in deionized water with the addition of citric acid, which acted as a dispersant. Crystalline monohydrate of citric acid was dissolved to obtain a 1.9-M aqueous solution and 2 wt. % of citric acid with respect to the solids loading was added after one hour of attrition milling. After milling the suspension was washed and centrifuged to remove the residual citric acid molecules by pouring of the supernatant. The sediment of the milled and citric-acid-coated TZ-3Y particles was re-dispersed in deionized water to obtain a 40 wt. % suspension. Note that the milled + citric-acid-coated core material will be denoted as TZ-3Y(CA) in the subsequent text.

3.3 Preparation of Y-TZP core-shell powder-blend slurry

With reference to the literature data in Section 1.3 the pH of the TZ-3Y(CA) core particles' slurry was adjusted to such a value that the agglomeration could be expected with a nano-sized suspension that was used in the as-received state at pH 3.2. The value ranged between pH 5 and 6.

The amount of shell particles needed to continuously cover the surface of the core particles was calculated and it is based on the average particle size of the core and shell particles. The equation and its derivation are detailed in Appendix A.

The agglomeration was performed in such a way that the suspension of shell particles was slowly added to the core suspension, in a drop-wise fashion, ensuring that the newly added nanoparticles had enough time to find a favorable place on the surface of the core particles.

3.4 Shaping of Y-TZP green bodies

Y-TZP core-shell powder-blend suspensions were wet-shaped by slip casting using plaster-of-Paris moulds to produce discs of 19 mm in diameter and 1.7 mm in height, and cylinders measuring roughly 4 mm in diameter and 6 mm in height. The as-received nanoparticle slurry was shaped only into cylinders, since the shaping of crack-free, nano-sized-powder discs is still an unresolved practical problem. In any case, after shaping all the samples were dried in air saturated with water vapor. The sub-micron-sized TZ-3YB powder supplied as a ready-to-press granulate was used as a reference material. The same sample geometries, both discs and cylinders, were prepared by dry-pressing using a uniaxial pressure of 147 MPa. Dry-pressing was used in order to achieve a similar green density as in the case of the wet-shaped powder blend.

3.5 Sintering: in air and in-situ in a TEM

3.5.1 CRH and Isothermal sintering

During the constant-rate-of-heating experiments (CRH) a contact-mode dilatometer (Bahr, Thermoanalyse) was used to monitor the densification of the Y-TZP powder blend, nano-sized Y-TZP and TZ-3YB powder compacts. The samples were sintered at a constant heating and cooling rate of 5 °C/min up to the end temperature without a dwell time. The end temperature was 1200 °C for the nanoparticle compacts and 1500 °C for the powder blend and the reference samples. The sintering schedule is shown in Figure 15.

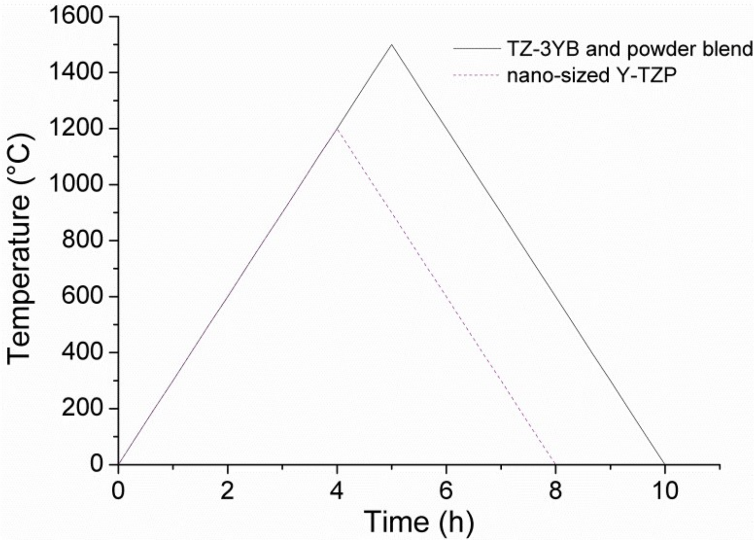

Figure 15: Sintering schedule used in the CRH experiments.

The discs subjected to sintering with a dwell time were divided into four groups that were sintered in temperature intervals of 100 °C, starting at 1000 °C and finishing at 1400 °C. The sintering was carried out in an ambient-air atmosphere at a heating rate of 5 °C/min with 2 hours of dwell time at each end temperature in an electrical resistance furnace (NABER, Germany). The sintering schedule with the introduced isothermal stage is presented in Figure 16.

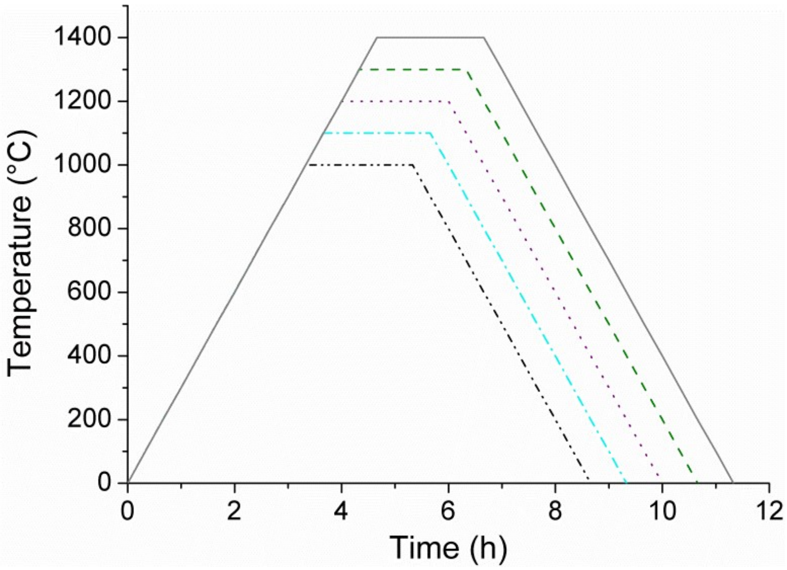

Figure 16: Sintering schedule used in the isothermal sintering.

3.5.2 In-situ heating TEM study

The core-shell powder blend for the in-situ heating TEM study was deposited on the platinum-sputtered, Ni-based TEM grid using a standard procedure. The experiment was conducted at a 5 °C/min heating rate and one-hour dwell time at the end temperature. The final temperature for in-situ TEM sintering was 1000 °C. The samples were sintered in increments of 100 °C, starting at 600 °C.

3.5.3 2D-sintering experiment

Samples used in the 2D sintering experiment, aimed at monitoring the pore-size evolution, were prepared using fully dense and thermally etched Y-TZP substrates sintered at 1450 °C for 2h in air with a 20-mm diameter and a 2-mm height. A drop of highly diluted suspension of Y-TZP nanoparticles was applied to the substrate's surface, which was subsequently dried at room temperature (XZO 1356/01, Mel Chemicals, Manchester). The samples were divided into thirteen groups that were sintered in temperature intervals of 50 °C, starting at 800 °C and finishing at 1400 °C. The sintering was performed in an ambient-air atmosphere at a heating rate of 5 °C/min, followed by a 2-hour dwell time at the end temperature (NABER, Germany). The surfaces were analyzed with an SEM (Carl Zeis, Supra 35LV, Oberkochen, Germany) in order to determine the sintering behavior of the nanostructured ceramics.

3.6 Characterization

3.6.1 Starting materials

The particle size distribution of the TZ-3Y starting material was measured using a particle size distribution analyzer (HORIBA, LA-920, France). Changes in the particle size distribution during the milling of the TZ-3Y starting powder with added citric acid were also followed. In order to determine the potential at the slip plane a zeta-potential analyzer (ZetaPals, BIC, USA) was employed. After the milling step the suspension was washed and centrifuged to remove the residual citric acid molecules. The quantity of adsorbed citric acid was determined by the titration of non-adsorbed acid in the supernatant of the milled core material using sodium hydroxide. Additionally, parts of the experimental results were confirmed by electron microscopy, i.e., transmission electron microscopy TEM (JEOL, JEM-2100, Japan) and scanning electron microscopy SEM (Carl Zeis, Supra 35LV, Oberkochen, Germany).

The particle size distribution of the as-received, nano-sized Y-TZP slurry was measured using dynamic light scattering measurements (DLS). The system is composed of an optical table, a thermostated water bath, a He-Ne laser (25mW at 632, 8 nm) and a digital correlator (ALV-6010/160). The measurements were performed in order to confirm the supplier's data about the particle size of the nano-sized Y-TZP and to study the effect of various pH values and various KCl concentrations on the hydrodynamic radius (r_H) of the nano-sized Y-TZP.

In all cases the pH values were adjusted using an ammonia solution (CarloErba) and acetic acid (CarloErba).

The TEM and SEM analyses were performed in order to visually confirm the success of the agglomeration and the uniformity of the shell particles' distribution attached to the surface of the core particles.

3.6.2 Biscuit-sintered ceramics: density and biaxial flexural strength measurements

The density of the biscuit-sintered samples was measured using Archimedes` method, where mercury was used as the immersion liquid.

The biaxial flexural strength method was chosen to assess the strength of the discs. The method is, according to ISO standard 6872:1995(E), appropriate for use with dental materials. According to R. Morrell[92] it can be used for specimens where the shape of the disc is the simplest form of test-piece that can be produced. Disc or square test-pieces are easier to prepare, especially under laboratory conditions, than bar test-pieces, and require less

machining. In addition, the edge preparation is less critical because the maximum stresses applied are remote from the edges.
In our case the measurement was performed with an Instron-1362 testing machine (Instron, USA), using a piston-on-three-balls test, at a loading rate of 1mm/min. The discs were symmetrically supported by three balls at one plane and loaded by a piston in the center of the opposite plane (Figure 17). The balls measure 3.2 mm in diameter and are placed in a circular configuration with a diameter of 11 mm. The piston has a diameter of 1.4 mm.

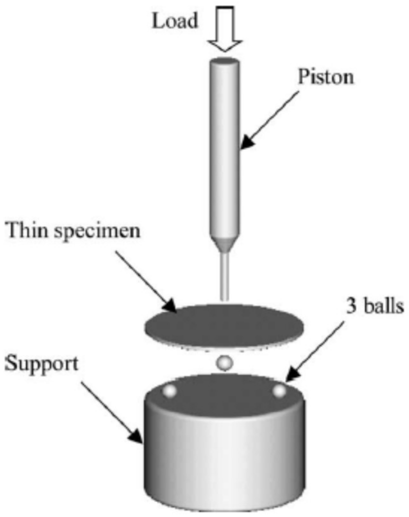

Figure 17: Piston-on-3-ball experimental configuration.

The samples were loaded until failure occurred and the force was registered in Newtons (N). The recorded value was inserted into the equation derived by Shetty et al.[93]

$$\sigma = -0.2387F(X - Y)/d^2 \tag{18}$$

where σ represents the biaxial flexural strength, F is the force at failure, d is the thickness of the sample (mm), and X and Y are:

$$X = (1+\nu)ln\frac{r_2}{r_3}^2 + (\frac{1-\nu}{2})(\frac{r_2}{r_3})^2 \tag{19}$$

$$Y = (1+\nu)[1 + \ln(\frac{r_1}{r_3})^2] + (1-\nu)(\frac{r_1}{r_3})^2 \tag{20}$$

Here, ν is Poisson’s ratio for Y-TZP, r_1 is the diameter of the supporting circle (mm), r_2 is the diameter of the piston (mm), and r_3 is the diameter of the sample (mm).

Due to the small number of tested samples the Weibull statistics were not used to evaluate the flexural strength measurements. Only eight samples were tested at each temperature.

The fracture surfaces were analyzed with the SEM (Carl Zeis, Supra 35LV, Oberkochen, Germany) in order to determine the sintering behavior of the powder-blend ceramics.

4 Results and discussion

4.1 Characteristics of the starting powders

A SEM investigation was used initially in order to verify the morphology of the as-received TZ-3Y powder. The micrograph in Figure 18 shows that the powder is granulated and that the granule sizes vary from 10 µm to 80 µm.

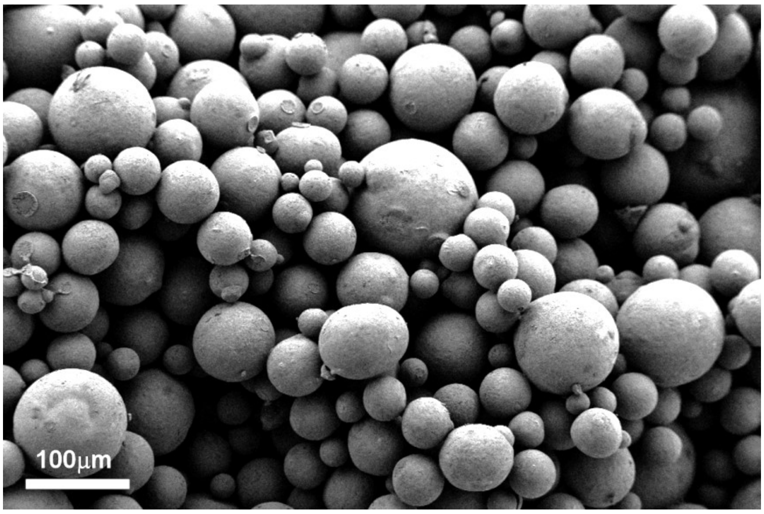

Figure 18: A SEM micrograph showing the TZ - 3Y granules. The granules measure from 10 µm to 80 µm.

The particle size of the powder was measured using a laser-scattering technique in such a way that a minute amount of the powder was added to the deionized water. The pH of the water was set to 3.5, with the aim of achieving electrostatic stabilization of the particles. Since the manufacturer's specifications state that the crystallite size measures 100 nm in diameter, ultrasound was used during the measurement in order to break down the granules. After 5 min of ultra-sonification the particle size distribution was measured, and it exhibited a d_{10} of 0.28 µm, a d_{50} of 0.72 µm and a d_{90} of 2.1 µm (Figure 19a). By comparing the specifications and the measurement results we were able to conclude that the powder is agglomerated since the d_{50} is far from the specified value for the crystallite size. This conclusion is supported by the TEM micrograph shown in Figure 19b, where the agglomerates of Y-TZP particles are evidenced.

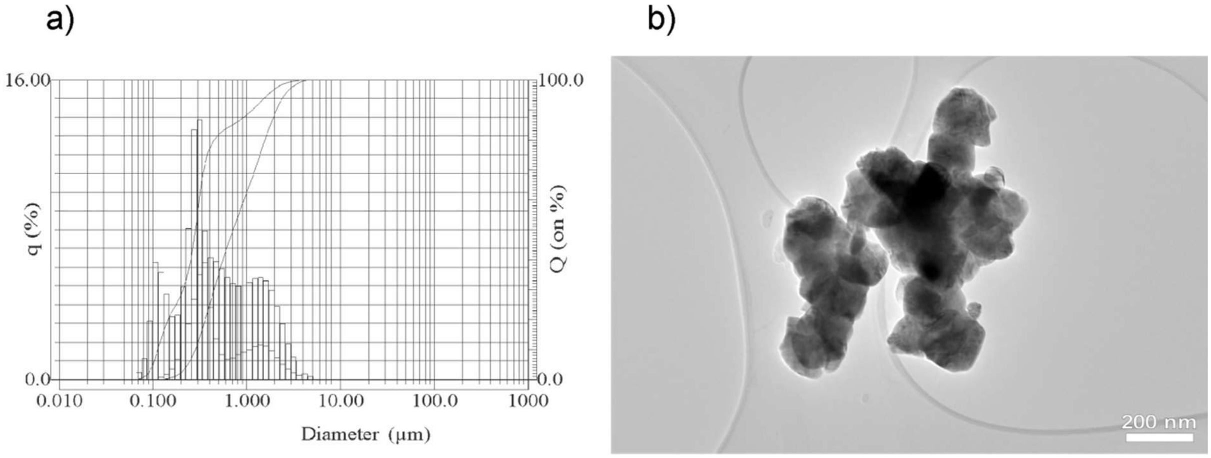

Figure 19: Characteristics of TZ-3Y powder before milling showing in a) Particles size distribution and in b) a TEM micrograph of the initial, as-received powder.

In order to achieve the highest level of deagglomeration the TZ-3Y powder was milled using an attrition mill. The milling was monitored continuously and the dependencies of the mean particle size and the pH on the time are shown in Figure 20. At the beginning of the milling the citric acid (CA) was added to the slurry and its two-fold action was exploited. It was used as a dispersant that enabled a high level of deagglomeration and, on the other hand, it also induced a shift of the IEP. The importance of the latter action will be detailed in subsequent sections. Upon the addition of CA the pH dropped from the naturally occurring pH 5.5 to pH 3. With time the pH value increases up to pH 6 and the particle size decreases, reaching a mean value of 0.2 μm after 170 min of milling. During the milling fresh surfaces of the powder are exposed, which bind the protons and the citric acid from the water, hence, the pH value of the slurry increases. In order to compensate for the increased specific surface area during the milling a surplus of citric acid was added at the beginning of the milling cycle.

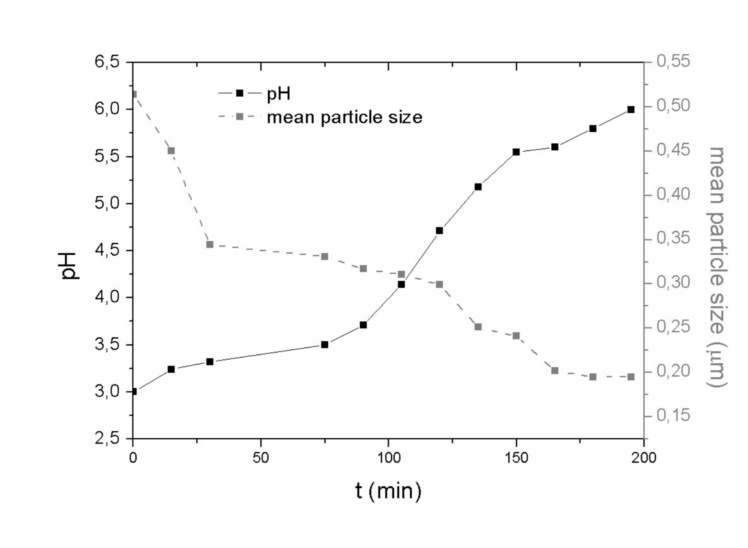

Figure 20: Dependence of pH and mean particle size of the aqueous slurry if TZ-3Y in the presence of CA on the time of milling. Note that citric acid was used as a dispersing agent.

After 200 min of milling in an attrition mill the residual dispersant was removed and after re-dispersion the material exhibited a mono-modal character with a d_{10} of 0.13 µm, a d_{50} of 0.19 µm and a d_{90} of 0.27 µm (Figure 21a). Its respective morphology was inspected using a TEM and the micrograph the shown in Figure 21b.

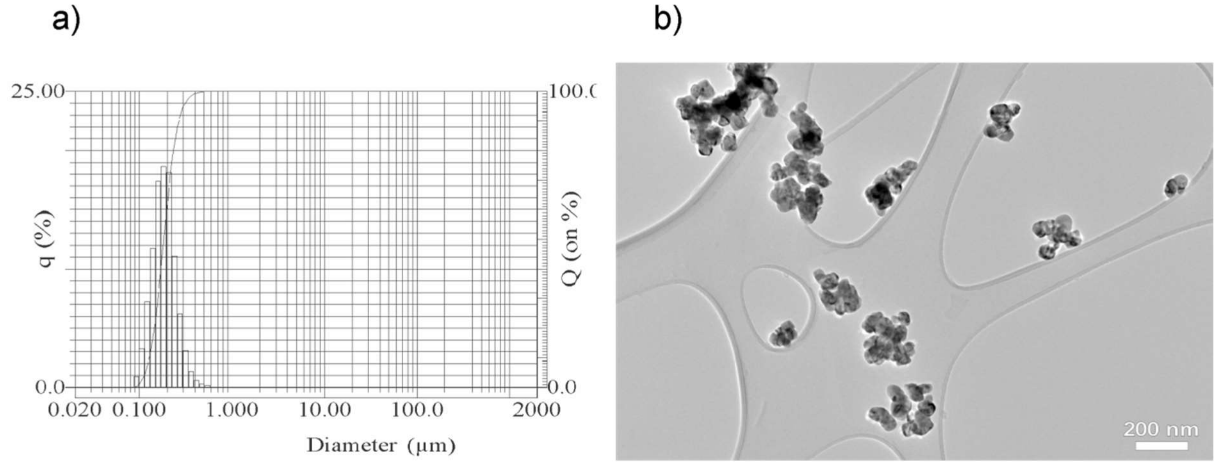

Figure 21: Characteristics of TZ-3Y(CA) powder after milling showing in a) Particles size distribution and in b) a TEM micrograph of the milled powder.

It has been shown that even when using an extensive attrition milling procedure the specified crystallite size was not reached, which indicates the presence of hard agglomerates. The mono-dispersed, particle-size distributions obtained from the laser-scattering measurements were satisfactori for the subsequent steps.

According to Hidber et al[94] a 0.4 wt. % of citric acid is needed to completely cover the surface of α-alumina particles with a mean particle size of 0.5 µm. Because during the milling of TZ-3Y the particle size is reduced below 0.5 µm a surplus of 2 wt. % of citric acid, with respect to solid loading, was added. Part of the CA adsorbs onto the Y-TZP particles' surfaces and part of it remains dissolved in the liquid part of the suspension. Direct titration was used in order to confirm the efficiency of the centrifugation and the re-dispersion step in removing the redundant citric acid molecules. Figure 22 shows the comparison of titration behavior of the core TZ-3Y(CA) suspension in the presence of the redundant citric acid (solid curve) and that of the TZ-3Y(CA) suspension that was subjected to centrifugation and re-dispersion in deionized water (dashed curve). The latter contains only adsorbed citric acid. As can be seen, both titration curves differ in the course of the pH change with the base addition. Whereas before the removal of the citric acid only characteristic pH transitions are observed, after the removal the pH increases linearly with the base addition evidencing the removal of dissolved citric acid in the latter case. It was determined by the titration of a core suspension supernatant that 0.9 wt% of citric acid with respect to the solids loading is enough for a full surface coverage of the wet-milled core, material reaching a particle size of 200 nm.

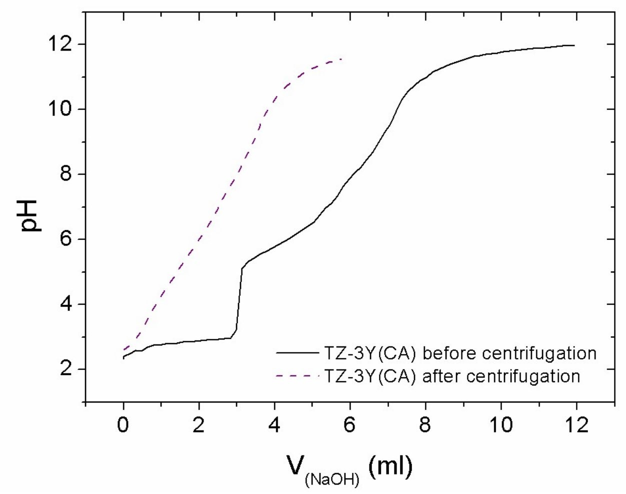

Figure 22: Titration curves of the core suspension before removal of citric acid surplus (solid curve) and after centrifugation and re-dispersion (dashed curve).

The particle size distribution of the shell nano-sized Y-TZP material suspension was determined by the TEM and DLS analyses. The TEM confirmed the manufacturer`s specification according to which an average particle size of 11 nm is present in the electrostatically stabilized slurry (Figure 23a). Since the TEM analysis is based on the agglomerates of nano-particles that form during the preparation of the sample, DLS measurements were also performed (Figure 23b). The method is similar to that used above for the routine particle size analysis; the difference is in the resolution. Details are given in Section 3.6.1. Using this method the hydrodynamic radius (r_H) of the nano-sized particles can be measured. At pH = 4.8 nm r_H measures 60 nm. By adding monovalent electrolyte, i.e., KCl, the r_H value is reduced to 40 nm at a 0.001-M concentration and to 11 nm at a 0.01-M concentration. If the concentration is further increased, i.e., to 0.1 M, the nanoparticles agglomerate and an r_H of 1000 nm was measured. Another test was performed with increasing the pH from 4.8 to 6.4, which again resulted in the nanoparticles' agglomeration, since the DLS showed a particle size of 900 nm at pH 6.4, indicating the instability of the nanoparticle slurry to pH changes.

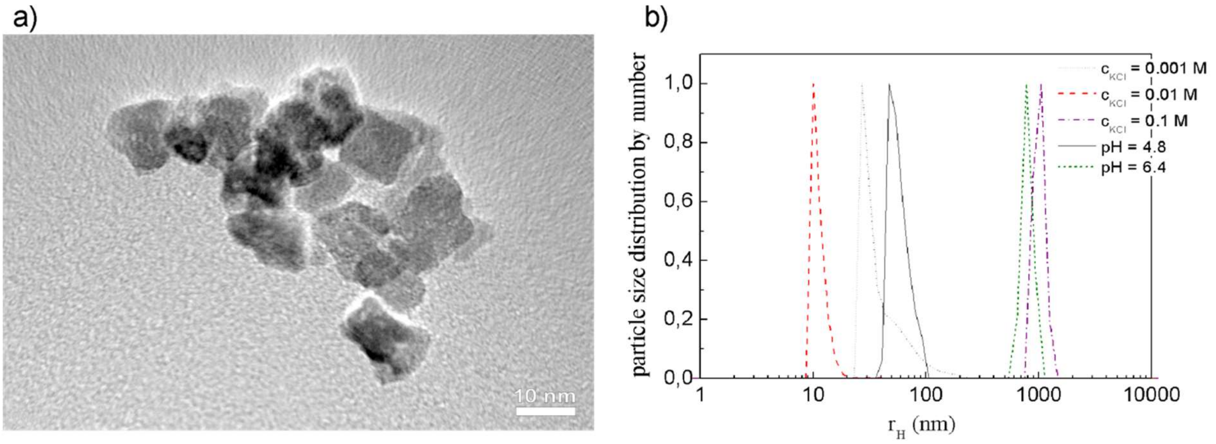

Figure 23: Characteristics of nano-sized Y-TZP showing in a) a TEM micrograph of an agglomerate and in b) a DLS analysis of the hydrodynamic radius (r_H) dependence on the concentration of the monovalent electrolyte.

The characteristics of the starting suspensions that are relevant to our work are given Table 2.

	pH	ζ potential (mV)	IEP	Particles size (nm)	Solids content (wt%)
TZ-3Y(CA)*	5-6	-40	2	200	40
NanoY-TZP**	3.2-4.20	+45	8	11	25

*TZ-3Y(CA) denotes TZ-3Y zirconia material with adsorbed citric acid (CA)

** Supplier's specifications. The pH of the slurry varied among different batches and it ranged from 3.2 to 4.2.

Table 2: Main characteristics of prepared starting suspensions of core and shell Y-TZP.

4.2 Electro-kinetic properties

The zeta-potential vs. pH curves for the core and the shell powders used in the agglomeration experiments are shown in Figure 24. Y-TZP materials, the core TZ-3Y and the shell nano-sized Y-TZP, exhibit an almost identical dependence of the zeta-potential on the pH with the IEP at pH = 8 (Figure 24a). In order to achieve a sufficiently high zeta-potential difference between the sub-micron-sized and the nano-sized Y-TZP, the surface properties of the core particles were modified by adsorbing citric acid (CA) onto the surface. The adsorption of 0.9 % of the CA results in a shift of the isoelectric point to pH 2, as shown in Figure 24b. Note that the denomination of the TZ-3Y after adsorbing the citric acid is changed to TZ-3Y(CA). According to the literature,[95,96] the shifted value of the IEP corresponds exactly to that of the SiO_2 and its zeta-potential vs. pH curve was also experimentally verified, as shown in the dashed curve in Figure 24b.

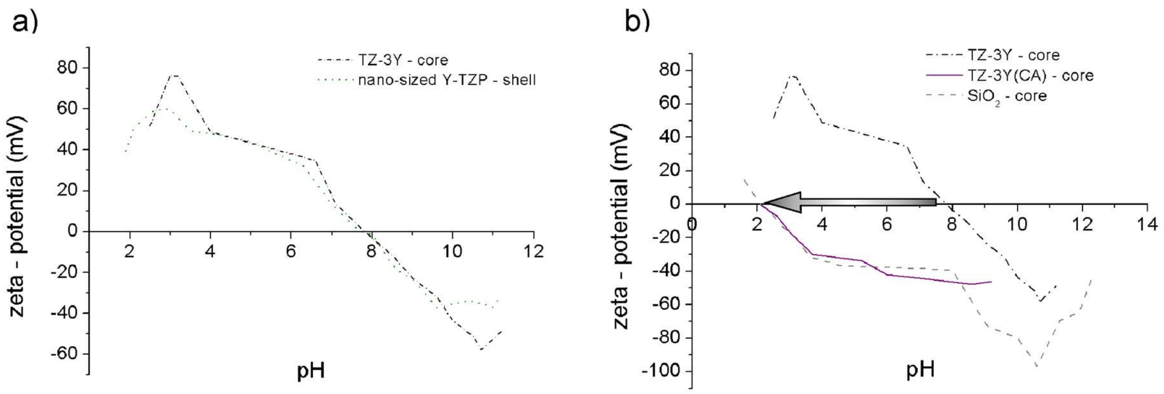

Figure 24: Zeta-potential vs. pH for four types of particle suspensions in a) the as-received core and shell Y-TZP materials and in b) the core SiO_2 and a shift in the IEP of the core TZ-3Y due to citric acid addition denoted as TZ-3Y(CA)

4.3 Preparation of core-shell powder blends

According to the DLVO theory and with reference to Figure 24b, the mixing of the CA-modified core Y-TZP slurry with a shell nano-sized Y-TZP slurry should result in both electrostatic and van der Walls (vdW) attractions in the pH range from 2 to 8. By inserting the experimentally determined values of the particle sizes, zeta-potential values and ionic strength of the powder-blend slurry into equations 1 and 5 in Section 1.3.3, the depth of the primary minimum at two arbitrarily selected inter-particle distances was obtained (Figure 25). The interaction potential at the inter-particle distances of 10 nm and 40 nm exhibits the most favorable absolute values for the agglomeration in the pH range from 3 to 6 where the highest surface coverage of coarser core particles with smaller shell particles should be achieved. As such, the powder-blend slurry was designed to have pH values between 4 and 5.

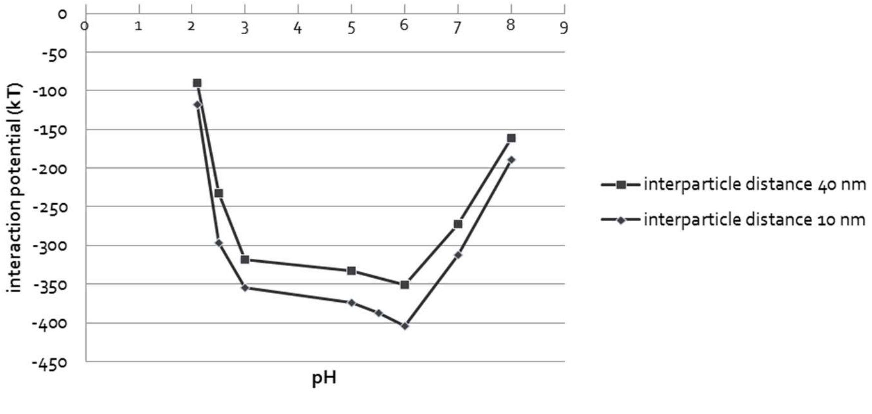

Figure 25: Calculated dependence of the interaction potential on the pH between the core and the shell particles at two different inter-particle separations

With reference to Figure 26, the process of agglomeration was conducted with distinct initial pH values, i.e., the nano-sized slurry had a pH = 3.5 and the submicron-sized a pH ≈ 6, so that after mixing the core-shell powder blend stabilized at the desired pH = 4.8. At this pH the absolute potential difference between the positively charged core and the negatively charged shell particles is the highest and a dense surface coverage of the core particles can be expected.

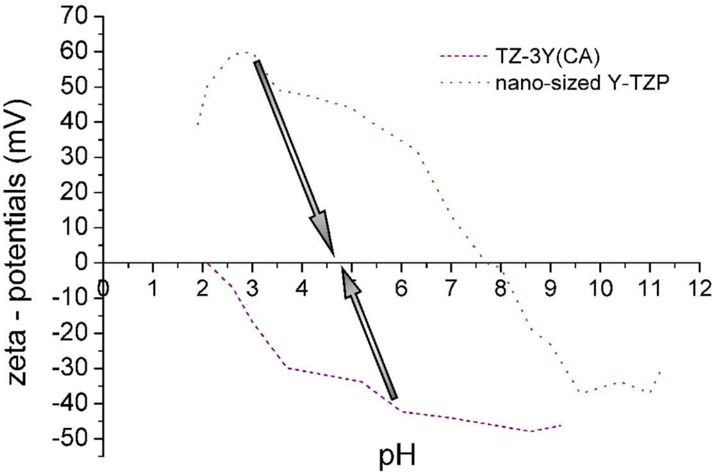

Figure 26: Dependence of the zeta-potential on pH for the combination of the surface-modified sub-micron-sized Y-TZP and unmodified nano-sized Y-TZP suspensions. The arrows indicate the pH at which the powder-blend material was prepared.

The TEM examination of the dried powder-blend slurry prepared at pH 4.8 was aimed at the verification of the efficiency of the agglomeration process. The analysis showed good surface coverage and a homogeneous distribution of nano-sized particles across the surface of submicron-sized core particles (Figure 27a). This result was later supported by an SEM analysis of the fracture surface of a green pellet after slip casting, showing a uniform distribution of shell particles across the whole surface (Figure 27b).

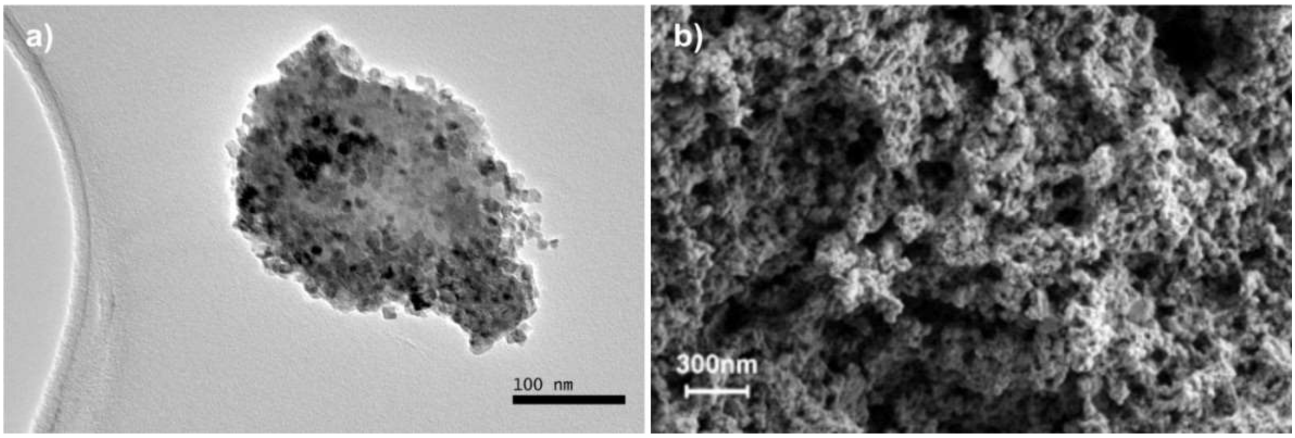

Figure 27: Analysis of homo-agglomeration showing in a) a TEM micrograph of a single TZ-3Y core-particle coated with nano-sized zirconia particles and in b) an SEM micrograph of the fracture surface of the slip-casted pellet with a homogeneous distribution of shell particles through the whole thickness of the green sample.

Finally, the agglomeration due to the electrostatic attraction between two particle sizes at various pH values was examined using a model system of core SiO_2 and shell nano-sized Y-TZP. In contrast to the Y-TZP core particles, the particle size analysis of silica core particles revealed a mono-modal distribution with a d_{10} of 0.31 µm, a d_{50} of 0.47 µm and a d_{90} of 0.60 µm (Figure 28a). An additional TEM investigation showed all these particles are perfect spheres of around 500 nm in diameter, as shown in Figure 28b. The analysis of the nano-sized particles is given above.

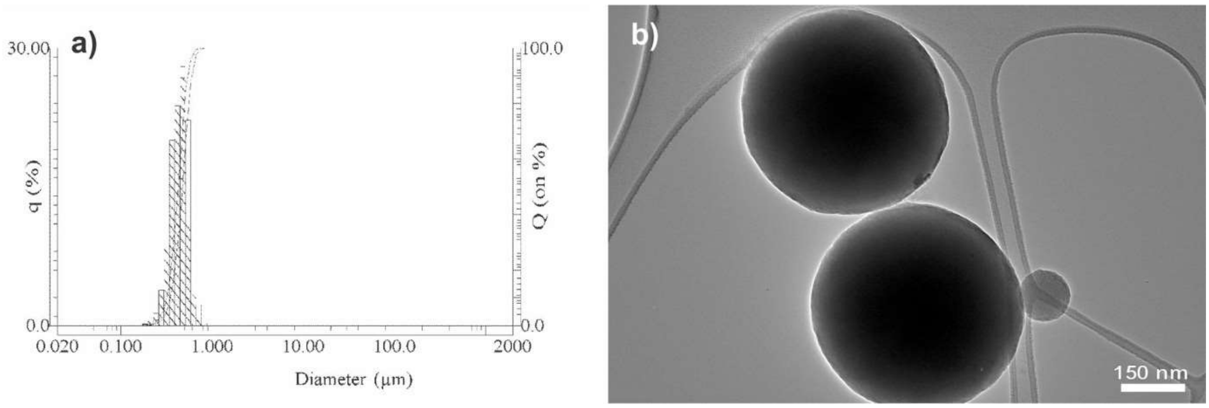

Figure 28: Characterization of SiO_2 starting material showing in a) particle size distribution using the light-scattering technique and b) the TEM micrograph of round, 500-nm particles accompanied by a smaller fraction measuring less than 100 nm in diameter

As shown in Figure 29a near the isoelectric point (IEP) of the core SiO_2 particles, i.e., at pH = 3, agglomeration took place with only a few shell Y-TZP particles attached to the core particles' surface. In contrast, at pH 4.8, where the absolute difference in the zeta-potential between both types of particles is the highest, the surface coverage of the core particles has increased substantially (Figure 29b). By approaching the IEP of the nano-sized particles, i.e., to pH = 7.1, the agglomeration between the nano-sized particles occurred and only occasional attachment onto the surface of the SiO_2 particles was observed (Figure 29c). By increasing the pH above the isoelectric point of the nano-sized Y-TZP, i.e., to pH = 9.1, the zeta-potential of both particle species gains a negative value and, consequently, a repulsive inter-particle potential prevents the attachment of the Y-TZP onto the surface of the SiO_2 (Figure 29d). The difference in the surface coverage between the core and the shell particles near either IEPs could be a consequence of the two intrinsic properties that are related to the particle size and suspension`s pH. First, according to the literature,[21] 10-nm spheres exhibit a 10^6 times higher rotational relaxation compared to 500-nm spheres and second at pH values near IEP a low repulsive inter-particle potential occurs for any type of particles in the slurry. It is therefore hypothesized that at pH 3 the velocity of the nanoparticles enables agglomeration between the core SiO_2 and the shell Y-TZP, previously agglomeration only between the core SiO_2 particles could occur. On the other hand, the destabilization of the nanoparticle slurry at pH 7 disables their attachment onto the surface of the core particles, leading to a preferential agglomeration between nano-sized particles.

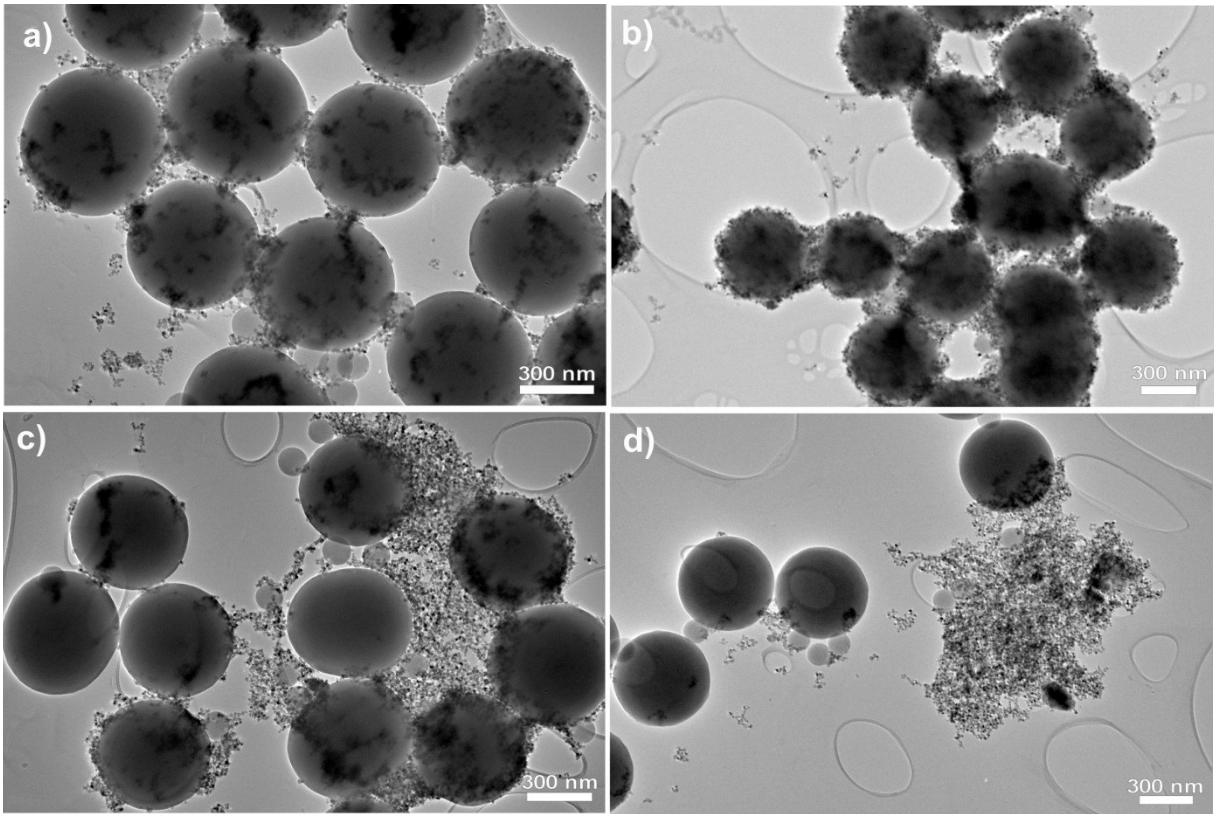

Figure 29: Dependence of surface coverage density of the model SiO_2–Y-TZP system on pH at a) pH=3, b) pH=4.8, c) pH=7.1 and d) pH=9.1

The TEM analysis after the agglomeration experiments at various pH values gave conclusive results indicating that the pH governs the agglomeration and that the highest surface coverage is achieved at pH = 4.8, where the absolute difference in zeta-potential values between the two particles species is the highest (Figure 24).

Although it has been shown that, in terms of electrostatic interactions, a pH value of 4.8 is the most suitable to perform agglomeration, still the surface of he core particles shown in Figure 29b has more unoccupied space than predicted by Equation A.3 (Appendix A). Since the hexagonally closed packed monolayer of shell particles attached on the surface of the core particles was not achieved, unbound nanoparticles exist in the final powder-blend slurry.

The phenomenon is most likely due to the relatively large hydrodynamic radius (r_H) of the nanoparticles. With reference to Figure 23b, at pH 4.8 the r_H was measured to be 60 nm. It was shown that by increasing the ionic strength of the slurry the double-layer thickness reduces and since it is directly related to r_H, the addition of monovalent electrolyte, i.e., KCl, was used. According to results of the DLS the ionic strength of 0.001 M reduces the r_H by 30 % to 40 nm and even more, i.e., to 11 nm, if the ionic strength is raised to 0.01 M. Therefore, the addition of monovalent electrolyte reduces the r_H and by that the far-reaching of inter-particle repulsion is also reduced, as shown in Figure 30. Based on this the nanoparticles are enabled to come closer, which should result in an increased surface coverage and the nearer position of the non-attached nano-sized particles to the core-shell complex.

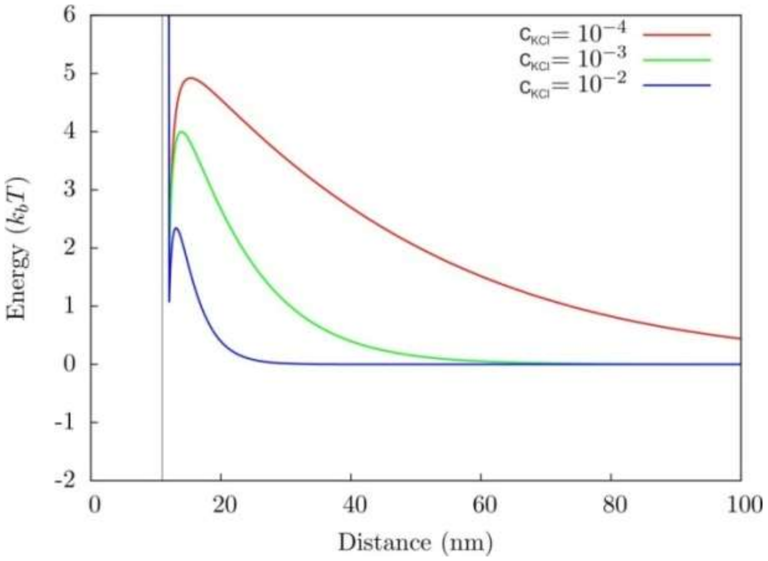

Figure 30: Calculated dependence of inter-particle potential on the distance between nano-sized particles.

The addition of electrolyte was expected to improve the surface coverage of the silica particles. However, a direct TEM analysis failed to provide a conclusive experimental confirmation of this assumption. Therefore, the hypothesis was tested using a Monte Carlo simulation (Appendix B).

4.4 Densification

The densification of the Y-TZP powder blend was assessed either during heating at a constant rate (CRH) or after sintering schedules, where an isothermal stage (dwell time) was introduced at selected end temperatures.

4.4.1 Shrinkage during a constant rate of heating

Shrinkage curves obtained during the CRH experiments of the three powder compacts are shown in Figure 31a. The specimens consisting of nano-sized particles after slip casting exhibited a green density of 51 % of TD and started to densify at 600 °C. They reached an almost theoretical density at 1200 °C. The green densities of the slip-casted, powder-blend slurry and the dry-pressed, sub-micron-sized powder exhibited a green density of 46 % of TD. The shrinkage of the powder-blend and submicron-sized powder compacts started at 800 °C and 900 °C, respectively, and reached their final density at 1400 °C and 1450 °C, respectively. The most remarkable difference in the shrinkage behavior among the three powder compacts occurs in the low-temperature region, i.e., between 600 °C and 800 °C, in which a slight shrinkage is observed in the case of the nano-sized compacts, whereas the other two materials do not show any noticeable shrinkage. Figure 31b shows the shrinkage rate of these three materials. The nano-sized powder compact evidently exhibits the highest shrinkage rate and the lowest temperature at which the maximum shrinkage rate is reached at 1050 °C. The other two materials shrink at a lower rate and reach the maximum rate of densification at 180 °C higher temperature, i.e., at 1230 °C. In the temperature interval between 800 °C and 1080 °C the powder-blend compact densifies at a higher rate compared to the sub-micron-sized material.

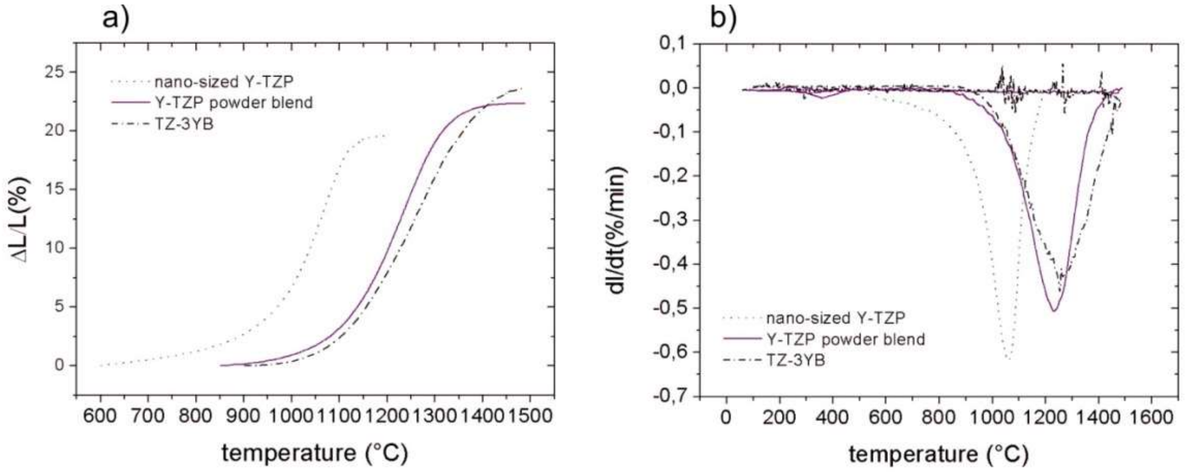

Figure 31: The CRH experiments showing in a) the relative density dependence on temperature and b) the shrinkage rate dependence on temperature.

4.4.2 Densification after sintering with an isothermal stage (dwell time)

The relative density values of the sintered discs of the Y-TZP powder-blend compacts obtained after 2 hours of isothermal sintering at various end temperatures are shown in Figure 32, together with the dry-pressed reference TZ-3YB material. The latter exhibits an almost linear increase of the relative density with temperature. At 1400 °C, a relative density of 98 % of TD is achieved. The powder-blend compacts, in contrast, exhibit a steady increase in the relative density up to 1100 °C, and from 1200 °C onwards, whereas between 1100 °C and 1200 °C there is a discontinuity, indicating that the presence of nanoparticles in the powder blend hinders the densification of the core material.

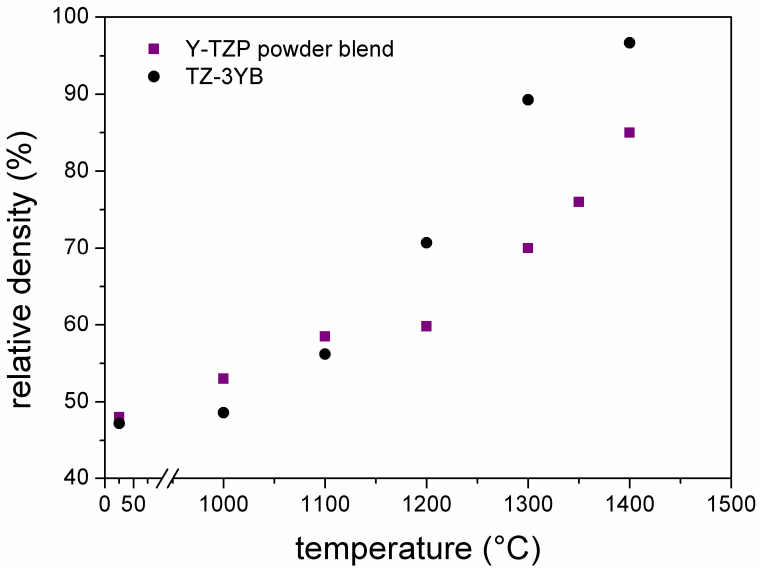

Figure 32: Variations in relative density with the sintering temperature of isothermal sintering (2 hours) for the TZ-3YB and Y-TZP powder blend.

In order to get better insights into the densification behavior during isothermal sintering at lower temperatures, in-situ-heating TEM experiments of the Y-TZP powder-blend material were employed. As shown in Figure 33a, the necking between nano-sized particles starts at about 600 °C, proceeds with the neck growth at 700°C (Figure 33b) and forming porous clusters at 800 °C (Figure 33c). At still higher temperatures, such as 900 °C, these clusters densify and literally move into the contact areas between the core particles (Figure 33d).

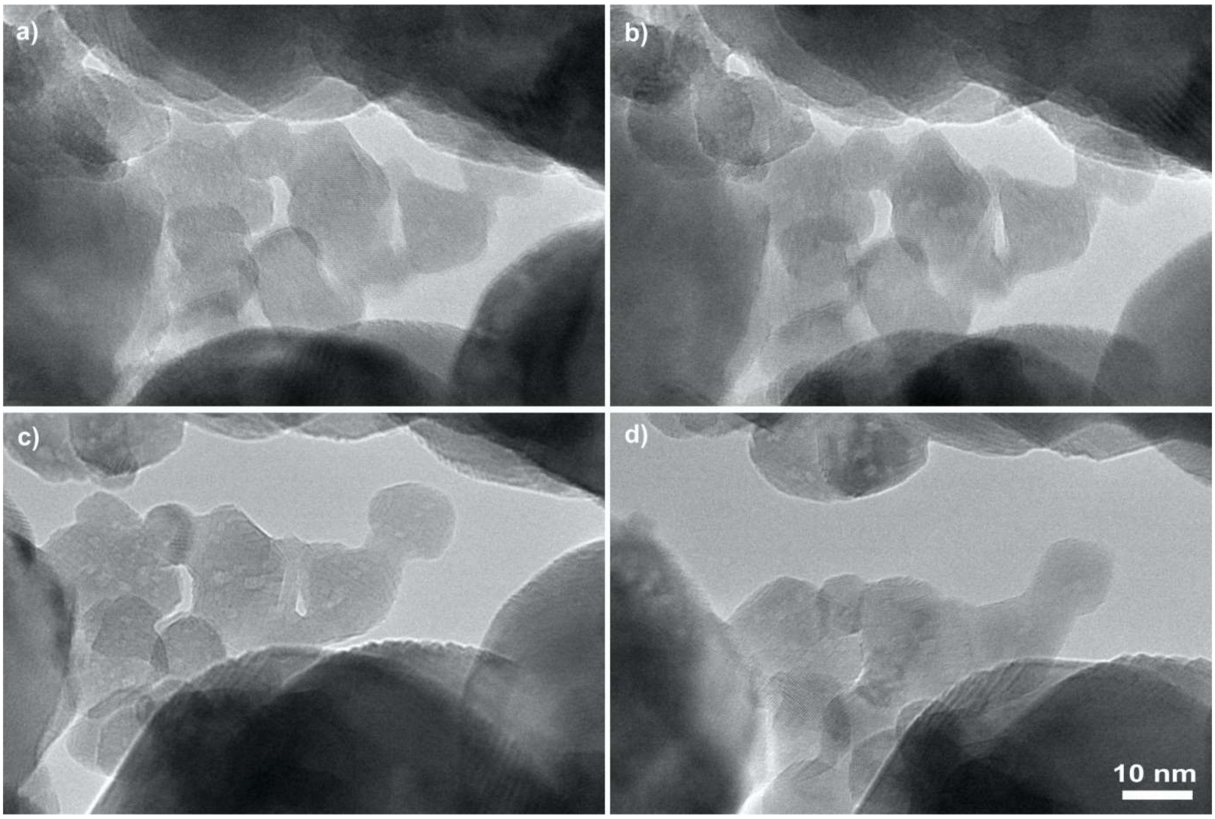

Figure 33: In-situ heating TEM study performed with 1h dwell time at a) 600°C where nanoparticles enter the initial stage of sintering, b) at 700°C where neck growth between nanoparticles can be observed, c) at 800°C where the movement of a sintered cluster has begun and d) at 900°C showing the movement of sintered nanoparticle cluster into the contact area between two core particles.

Consequently, before the nanoparticles are “swallowed” by the larger core particles due to the Ostwald ripening mechanism, all the stages of sintering between the nano-sized particles will occur. By gradually increasing the end temperature from 600 °C to 900 °C in 100 °C increments, only the nanoparticles are sinter-active forming partially sintered clusters (Figure 33 a-d). By introducing the dwell time into the sintering schedule, the sintered clusters have enough time to move into the contact areas between the core particles, thereby reducing the curvature between them (Figure 33d). The consequence of the migration is a reduced driving force for the diffusion mechanisms occurring during the sintering of the core particles and the densification of the powder blend is impeded up to 1200 °C (Figure 32). At higher temperatures the beneficial effect of the nanoparticles is lost and the densification of the powder blend proceeds as in the case of the core powder compact. Figure 33a also shows the onset of the diffusion processes by forming necks between the nanoparticles at temperatures as low as 600 °C. At 900 °C the clustered nanoparticles bridge the core particles by forming their polycrystalline neck. Even when increasing the end temperature to 1000 °C no interaction between the sintered clusters of nanoparticles and core particles could be observed. Therefore, a single nanoparticle attached to the surface of the sub-micron-sized particle was observed (Figure 34). The dynamics of the events were evidenced by successive TEM micrographs taken at different time intervals in the heating stage at 1000 °C. Figure 34a shows the neck formation between the core and shell particle after 30 min. After 40 min the majority of nano-sized particles are “swallowed” by the core particle (Figure 34b), and after 1h the complete integration of a particular single nanoparticle, which was initially adsorbed onto the core particle’s surface, is shown (Figure 34c).

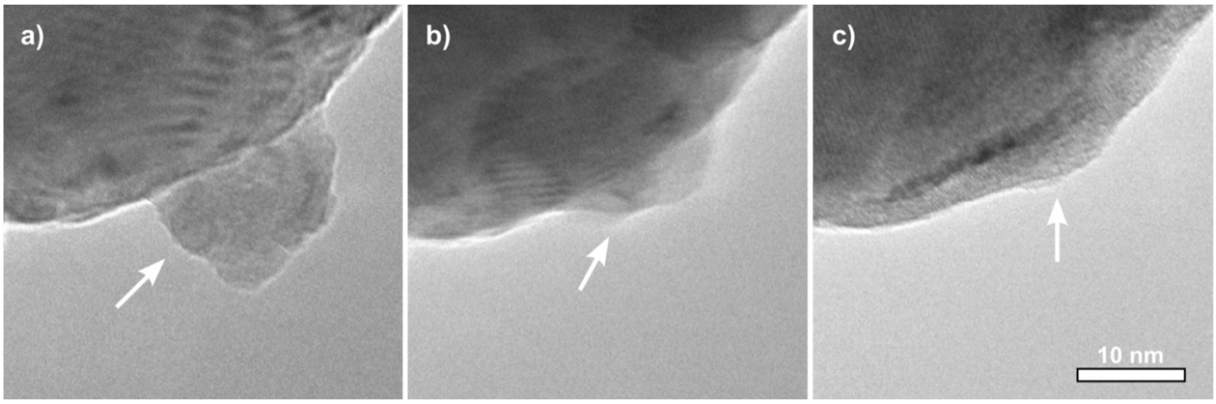

Figure 34: In-situ heating TEM study of the Y-TZP – Y-TZP powder blend at 1000°C showing a time sequence of nanoparticle incorporation into a core particle at a) 30 min, b) 40 min and c) 60 min.

The data obtained from the in-situ-heating TEM study led to the conclusion that the powder-blend material with a bimodal particle size distribution in the core-shell configuration represents a unique situation in sintering. As long as the activation energy of the coarser fraction is not reached during the heating, the finer particles in contact will sinter to form clusters. During the dwell-time step in the sintering schedule these clusters will migrate into the contact areas between the larger core particles. Furthermore, the densification between the smaller shell particles and larger core particles begins after they are positioned in the contact areas. As opposed to the dry-pressed, core-powder compacts where the necks are formed only between the submicron-sized particles, in the case of the core-shell powder blend exhibiting a bimodal particle size distribution, the nanoparticles contribute to the formation of necks.

4.5 Bi-axial flexural strength

As shown in Figure 35, the bi-axial flexural strength of biscuit-sintered Y-TZP fabricated from the powder blend is significantly higher than that obtained with dry-pressed and biscuit-sintered core Y-TZP powder exhibiting a similar fractional density. With reference to Figure 35, the steepest increase in strength of the powder-blend material is obtained by slight densification from 58 % TD to 60 % TD, which corresponds to the sintering in the temperature interval from 1100 °C to 1200 °C. The strength increase from 200 MPa to 420 MPa is remarkable. On the other hand, the reference core material exhibits practically the same biaxial flexural strength in the same density interval, i.e., roughly 150 MPa. With further densification up to 70 % of TD, achieved at the temperature of 1300 °C, the strength increases to 685 MPa, where a plateau is reached (Figure 35). Further increases in the fractional density to 85 %, resulted in an increase in the standard deviation, while the mean strength value remained relatively constant.

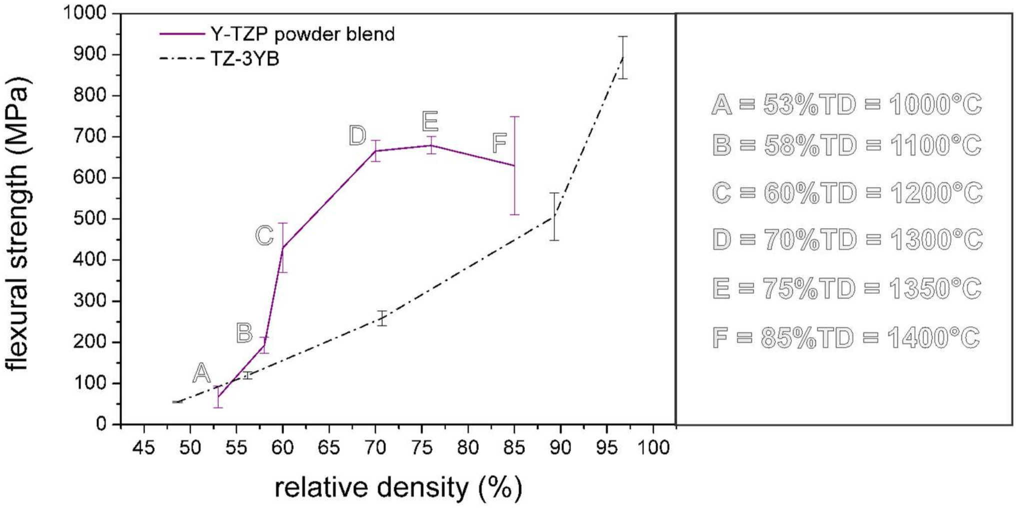

Figure 35: Biaxial flexural strength vs. relative density for powder-blend ceramics along with a comparison curve of biscuit-sintered TZ-3YB.

The initial hypothesis was that the added nanoparticles should increase the area of the strength-determining inter-particle contacts and indeed the values of the flexural strength of the biscuit-sintered, powder blend ceramics are significantly higher than the dry-pressed and biscuit-sintered core Y-TZP powder exhibiting a similar fractional density. The difference between the two materials is most pronounced with specimens having a moderate porosity (e.g. 40–20 %). The SEM analysis of the fracture surfaces showed that at 1000 °C only small neck areas have formed between the nanoparticles (Figure 36a), i.e., at 53 % of TD, which nicely corresponds to the low flexural strength. By taking into account the migration of nanoparticle clusters toward the neck areas between the sub-micron-sized core particles and the low flexural strength, we can conclude that at 1000 °C the sintered clusters still made no bond with the core particles. A density increase from 53 % TD to 58 % TD can be attributed to the movement and densification of the nanoparticles clusters and also to some extent to the densification with core particles, since a strength increase was recorded. In contrast, a minimal densification from 58% TD to 60% TD results in the remarkable increase in the strength (Figure 36b and c). As opposed to the dry-pressed, core powder compacts, where necks are formed only between submicron-sized particles, in the case of the powder blend, where the nanoparticles move into the neck area between sub-micron-sized particles enable the formation of necks between nano-sized and submicron-sized particles. Consequently, the flexural strength is increased without considerable densification of the sample. Hardy et al.[9] reported that before any densification the formation of necks between particles by surface diffusion can increase the mechanical properties, such as flexural strength, elastic modulus and fracture toughness. Thus the number of inter-particle contacts per unit area governs the final strength of the biscuit-sintered samples. The highest strength value was recorded after sintering at 1300 °C, i.e., at 70 % TD, where the nano-particle clusters became incorporated into the necks between the sub-micron-sized material. Up to this relative density the area of inter-particle contacts must have been increased without any pore coalescence (Figure 36d). Above 70% TD the strength remains essentially constant up to 85 % of TD. This plateau in strength could be attributed to the evolution of strength-determining flaws due to the coalescence of pores, which can be anticipated from the in-situ heating TEM study, where it was shown that the movement of nanoparticle clusters leaves an empty space behind and is also evident from higher values of the standard deviation at 85 % TD (Figure 36d).

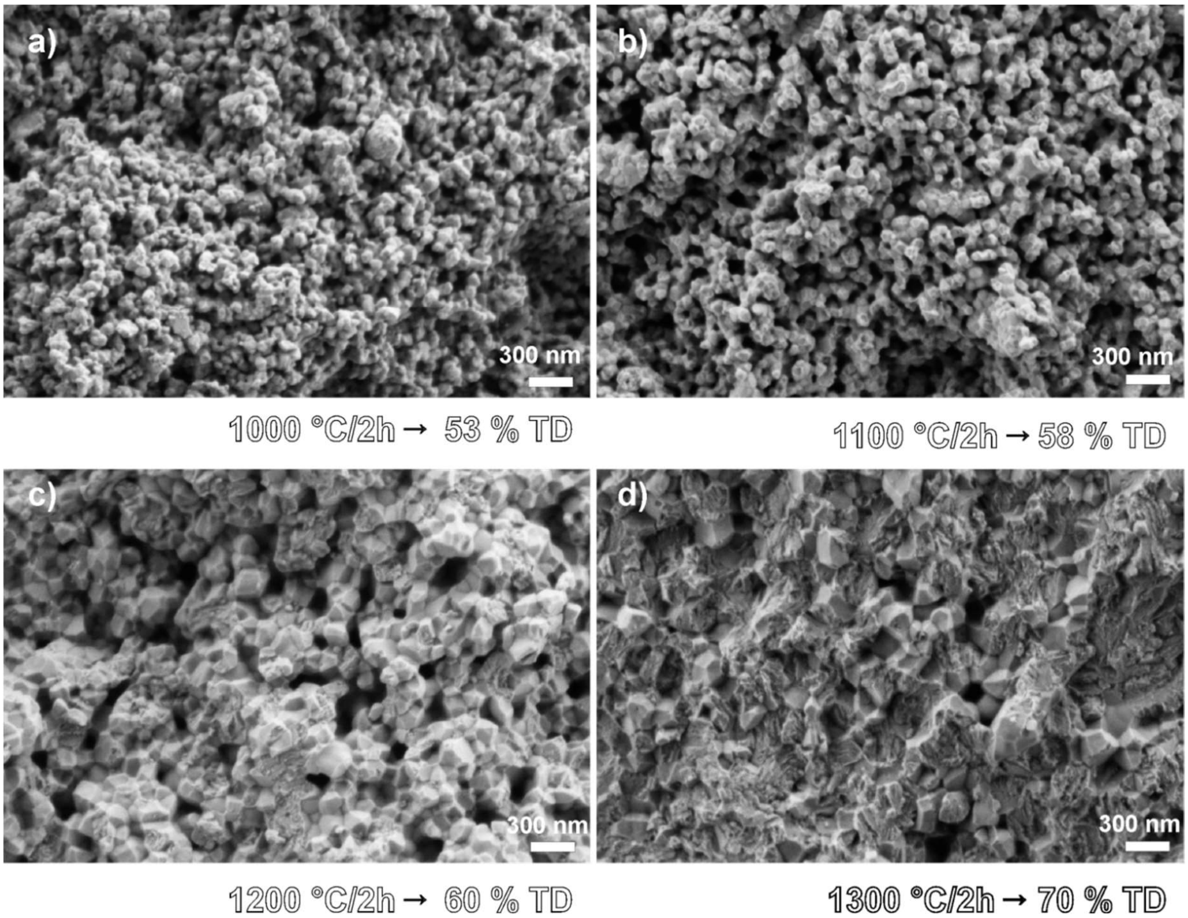

1000 °C/2h → 53 % TD

1100 °C/2h → 58 % TD

1200 °C/2h → 60 % TD

1300 °C/2h → 70 % TD

Figure 36: FEG-SEM analysis of fracture surface of the sample a) sintered at 1000°C, b) sintered at 1100°C, c) sintered at 1200°C and d) sintered at 1300°C.

Since the coalescence of pores could not be evaluated from the above analysis of the fractured surfaces, a simple 2D sintering experiment was designed, aimed at an observation of the growth of strength-determining pores.

In this experiment a uniform distribution of the nanoparticles in the core-shell material was considered, as schematically shown in Figure 37. The samples were prepared using densely sintered and thermally etched Y-TZP discs of 20 mm in diameter and 2 mm in height. A drop of a highly diluted suspension of Y-TZP nanoparticles was applied to the substrate surface, which was subsequently dried at room temperature.

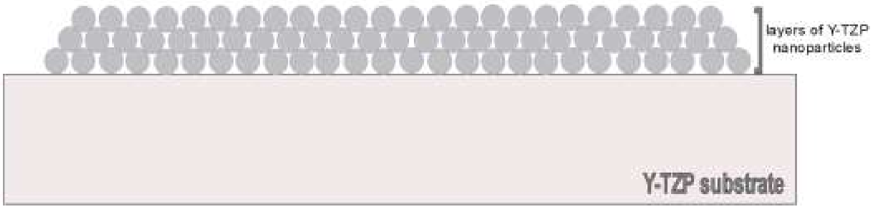

Figure 37: Scheme of the 2D sintering experiment.

After drying, the samples were sintered under same conditions, i.e., end-temperatures and dwell times, as the bulk samples exhibiting strength values of 68 MPa, 200 MPa, 420 MPa and 685 MPa shown in Figure 38a, b, c and d, respectively. The SEM micrographs taken from the surfaces of samples sintered for 2 hours at 1000 °C, 1100 °C, 1200 °C and 1300 °C are shown in Figure 38a, b, c and d. After sintering at 1000 °C a uniform distribution of nanoparticles that have probably entered the intermediate stage of sintering, according to the in-situ-heating TEM, is shown in Figure 38. After sintering at 1100 °C, the substantial grain and pore growth can be seen, but no pore coalescence to larger pores is observed (Figure 38b).

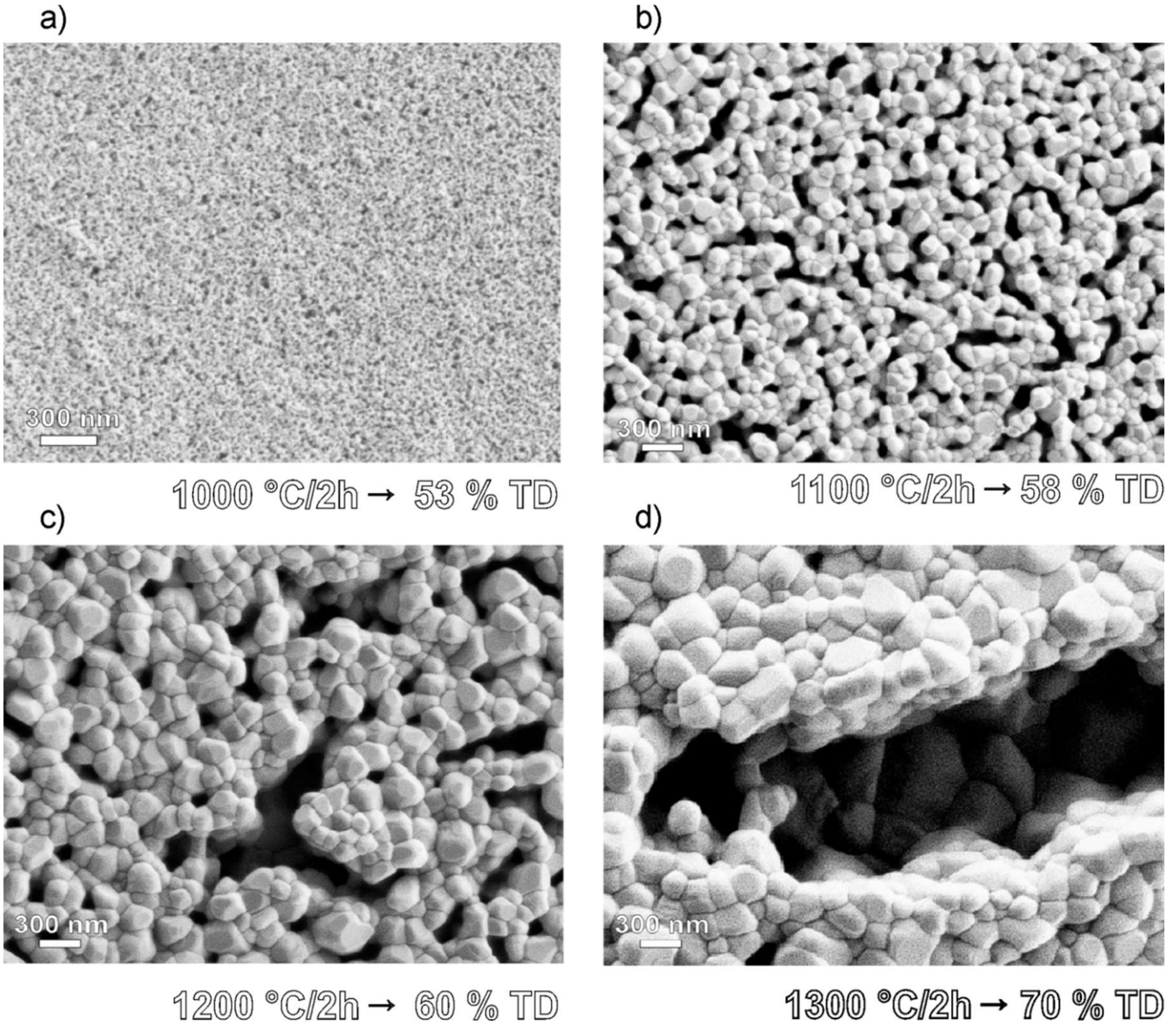

Figure 38: SEM-based sintering study of pore growth in a 2D situation showing a) flexural strength dependence on relative density and the corresponding samples sintered at b) 1100°C, c) at 1200°C and d) at 1300°C.

At 1200 °C further grain growth is accompanied by a marked pore coalescence (Figure 38c), whereas at 1300 °C the pores are already so large that they may become strength determining if they were in the bulk. Assuming that a similar mechanism is operating in the bulk samples, it is likely that these large pores are responsible for the plateau of the flexural strength, shown in Figure 38a. In the literature one can find statements that the pore size remains constant up to 83 % of the relative density,[66] while others claim that along with the grain growth the total number of pores will be reduced, but their average diameter and length will increase as a consequence of coalescence,[97] giving support to our results. It is important to be aware of the effects of constrained sintering in a thin surface layer of nano-sized particles, but nevertheless the results are in agreement with the results on flexural strength.

The effect of the porosity content on elastic modulus was not recorded due to the limited sample size that could be achieved using slip casting.

5 Summary and Conclusions

5.1 Colloidal processing

The attrition milling of TZ-3Y in the presence of citric acid is an effective method for reducing the particle size from the initial 780 nm to final 200 nm. Due to increases in the specific surface area during milling a surplus of citric acid was added that needed to be removed after the milling was completed. The efficiency of the centrifugation and re-dispersion was confirmed using a direct titration method, since characteristic pH transitions upon base addition are absent. It was determined that 0.9 wt. % of citric acid adsorbs onto the surface of the TZ-3Y particles with a mean particle size of 200 nm.

Citric acid was used intentionally during the milling in order to induce a shift in the IEP from the initial pH 8 to pH 2 of core Y-TZP particles. Consequently, the oppositely charged core and shell particles exhibit a primary minimum in the same pH range, which was evidenced by the calculation using equations from the DLVO theory. Mixing of both core and shell Y-TZP slurries resulted in the uniform distribution of nanoparticles on the surface of sub-micron-sized particles in the core-shell configuration. The extensive TEM analysis revealed that at pH 4.8 the highest surface coverage of core particles is achieved.

5.2 Densification and strength

The densification of the Y-TZP powder blend in a core-shell configuration was reduced compared to the sub-micron-sized core material during isothermal biscuit-sintering. This was due to the reduced curvature between the core particles, caused by the nanoparticles that fill the neck areas between them during sintering. At the same time, an enhanced neck growth resulted in a higher strength in the moderate porosity range. During the constant rate of heating (CRH) treatment, in contrast, these phenomena were not observed because the crucial stage of retarded densification, i.e., the migration of nanoparticles into the neck area between the coarser particles, did not occur.

Overall, the initial hypothesis was confirmed since the improvement in the mechanical properties of porous Y-TZP ceramics through the preparation of core-shell material was shown. The result confirms the initial assumption that the addition of nanoparticles results in a larger area of inter-particle contacts, thereby increasing the strength of nanostructured material. At a theoretical density of 70% the flexural strength almost doubles with respect to conventionally used dry-pressed micron-sized Y-TZP powder.

Although our 2D SEM model does not take into account the effects of constrained sintering, we believe that from the sintering experiment of the nano-sized powder spread onto the sintered Y-TZP substrate it can be concluded that a plateau of strength is reached due to the evolution of the strength-determining flaws by extensive pore growth.

6 Acknowledgments

These four and a half years have been quite life transforming. I came as a dentist and I am leaving with a lot of knowledge about dental ceramic materials. I would like to sincerely thank my mentor, prof. dr. Tomaž Kosmač, for having the courage to employ a dentist as a young researcher in the field of pure material science. If he had decided otherwise I would not have gained such a wealth of knowledge, not only about materials but also relating to a critical outlook regarding other fields of dentistry. Many decisions that I have to make as a practicing dentist are now easier because of the knowledge I gained at the JSI. I would also like to thank my co-mentor, dr. Aleš Dakskobler, for many valuable discussions and for directing my thoughts, usually in the right direction. During my PhD we became good friends and I sincerely hope that the friendship will last into the future.

I shared the office with two great guys who I have the deepest respect for. They are already doctors. Dr. Andraž Kocjan is currently a post-doc in Stockholm, and dr. Aljoša Maglica is working at the company LEK. Andraž thank you for becoming my great friend, for taking time to discuss personal and scientific topics, and for being the support each young researcher should have. Aljoša, as for Andraž, the same goes to you, we were a good team and it is so in life that our careers diverged but, nevertheless, I am convinced that we will stay in touch. Next is Lovro Gorjan, who is at the moment under a similar pressure to me; he is also writing his thesis. Lovro, thank you for the valuable discussions about material science. Martin, our youngest associate, thank you for keeping me company.

Thank you dr. Irena Pribošič for performing the crucial in-situ heating TEM analysis and thank you dr. Kristoffer Krnel for valuable discussions during the first year of my PhD.

Thank you also to Darko Eterovič, Tomislav Pustotnik, Natalija Petkovič and Mojca Hren for the support that I needed with various experimental set-ups and other paper work.

I would like to thank dr. Sašo Gyergyek, dr. Gregor Trefalt and dr. Milan Ambrožič for valuable discussions and to all the others who in anyway contributed to this PhD thesis.

A thanks also goes to my family, for their patience and moral support during these four and a half years.

Finally, I would like to thank you Maruša for supporting me in the moments when the stress was just too much to bear and for bringing objectivity to my reasoning when it was needed.

7 Appendix A

With the help of the physicist dr. Milan Ambrožič, a simple equation was derived aimed at keeping the ratio of the core-to-shell fraction constant, regardless of the inhomogeneity in the particle sizes. The question was raised: what is the quantity of shell particles needed to continuously cover the surface of core particles in one continuous layer?

Assuming that all the particles are perfect spheres and that one layer of nano-sized particles is attached to the surface of sub-micron sized particles, then by using equations for the surface area we get:

$$N\pi r^{2} = k4\pi R^{2} \qquad \text{A.1}$$

where *N* is the total number of smaller particles that can cover the surface of a core particle, *k* is the factor of surface coverage of core fraction (for shell particles we take the areas of spherical main cross-sections and not the area of the spheres since we are interested in core particle surface covering), R and *r* are the radii of core and shell particles, respectively.

The surface coverage factor k depends essentially on the 2D geometry of the circles on the 2D square that represents the spread out surface of the sphere. In the case of the close-packed structure of circles in an infinite plane the surface coverage factor *k* has a value of 90.7 %. This value holds for circles that cannot penetrate each other and have neutral surface charge. Using equation A.1 for *N*, we can calculate the volume ratio of both types of particles:

$$\frac{V_s}{V_c} = \frac{4N\frac{\pi r^{3}}{3}}{4\frac{\pi R^{3}}{3}} = \frac{4k\ \ ^{2}}{r^{2}} * \frac{r^{3}}{R^{3}} = \frac{4kr}{R} \qquad \text{A.2}$$

If monolayer covering of core spheres with much smaller shell particles is assumed, the weight ratio of the two types of particles can be determined by the following equation:

$$\frac{m_c}{m_s} = \frac{\rho_c R}{\rho_s k 4r} \qquad \text{A.3}$$

R, *r*, ρ_c and ρ_s are, respectively, the radii and densities of core and shell particles.

8 Appendix B

Monte-Carlo simulation of SiO_2 - Y-TZP powder-blend system

While preparing core-shell powder blend slurries a surface coverage factor k of 0.91, was predicted for monolayer of hexagonally close-packed nanoparticles. As the TEM analysis indicated the achieved k was lower and because there are no experimental methods to verify it, a Monte-Carlo simulation was used. At first the simulation was aimed at verifying whether the chosen surface coverage factor k = 0.91 in reality represents the amount of nano-particles that are firmly attached to the surface of the sub-micron-sized SiO_2 particles. Secondly, if the k factor value is lower than expected, the question is where the surplus shell particles remain. The experimental data on particle size, zeta-potential values and solid loadings were used. Furthermore, the DLS measurements on the hydrodynamic radius ($_{rH}$) value of nanoparticles indicate that the addition of monovalent electrolyte reduces its value, which could be a plausible solution for increasing the surface coverage factor k.

The three-dimensional Monte-Carlo technique at finite temperature was employed[98, 99]. The particles in the suspension are assumed to be a charged hard spheres in a continuous medium. Water molecules and ion species in the suspension are not modeled explicitly, only their average contribution on the colloid-colloid interactions is taken into account. The DLVO interaction potential was used to model the interactions in these systems and is described in greater detail in the introduction.

The canonical ensemble with the fixed number of particles N, volume V, and temperature T was used. The temperature is fixed to T = 298 K and the total number of particles in the simulation cell is 1100. The cubic simulation cell with the periodic boundary conditions and the minimum image convention were employed.[100] The volume of the simulation cell was calculated from the volume concentrations (Φ) of the particles and the number of the particles in the simulation cell.

In all the simulations we kept the concentrations of the particles the same as in the experiments. The core slurry in the model system contains Φ_{SiO2} = 4 vol. % and in the Y-TZP – Y-TZP system Φ_{ZrO2} = 10 vol. %. In both cases the $\Phi_{\text{nano-sized Y-TZP}}$ = 5.5 vol.%. Surface charge values were taken from the corresponding zeta-potential values that were adopted from the experimental data at pH 4. One has to be aware that Y-TZP – Y-TZP system cannot be directly connected to the simulation results since core particles are irregularly shaped. Therefore, the results are applicable to the model SiO_2 – Y-TZP system only. The values used are summarized in

Table 3.

material	pH	R [nm]	Ψ [mV]	H* [J]	$\kappa_{c=10^{-3}M}$ [m^{-1}]	$\kappa_{c=10^{-2}M}$[m^{-1}]	$\kappa_{c=0.1M}$ [m^{-1}]
Y-TZP	4	186	- 38	$7.23*10^{-20}$ J	$1.03*10^8$	$3.26*10^8$	$1.03*10^9$
Y-TZP	4	11	+ 48	$7.23*10^{-20}$ J	$1.03*10^8$	$3.26*10^8$	$1.03*10^9$
SiO_2	4	500	-44	$0.46*10^{-20}$ J	$1.03*10^8$	$3.26*10^8$	$1.03*10^9$

Table 3: The data used for Monte Carlo simulation.

* H denotes Hamaker`s constant and index at κ indicates the electrolyte concentration that was used during simulation.

The results of the simulation on 4 vol. % of core SiO_2 slurry are given in Figure 39. Surprisingly, the actual surface coverage factor k reaches the value of only 0.05 for electrolyte concentrations of 10^{-4} M, it increases to 0.14 at electrolyte concentration of 10^{-3} M and it reaches a value of 0.26 at 10^{-2} M as shown in Figure 39a. The simulation showed that surface-coverage factor k is indeed influenced by r_H. Furthermore, an estimate on the position of remaining non-attached nanoparticles still present in the powder blend slurry was obtained (Figure 39b). As it seems the position of the next-nearest nanoparticle is also determined by r_H value, so with increasing the ionic strength not only that higher surface filling can be achieved but also the overall proximity of non-adhered nanoparticles is increased, which could contribute to their improved distribution after shaping. Figure 39c is graphically presenting the results of the calculation and one can indeed observe a higher surface coverage with higher electrolyte concentrations.

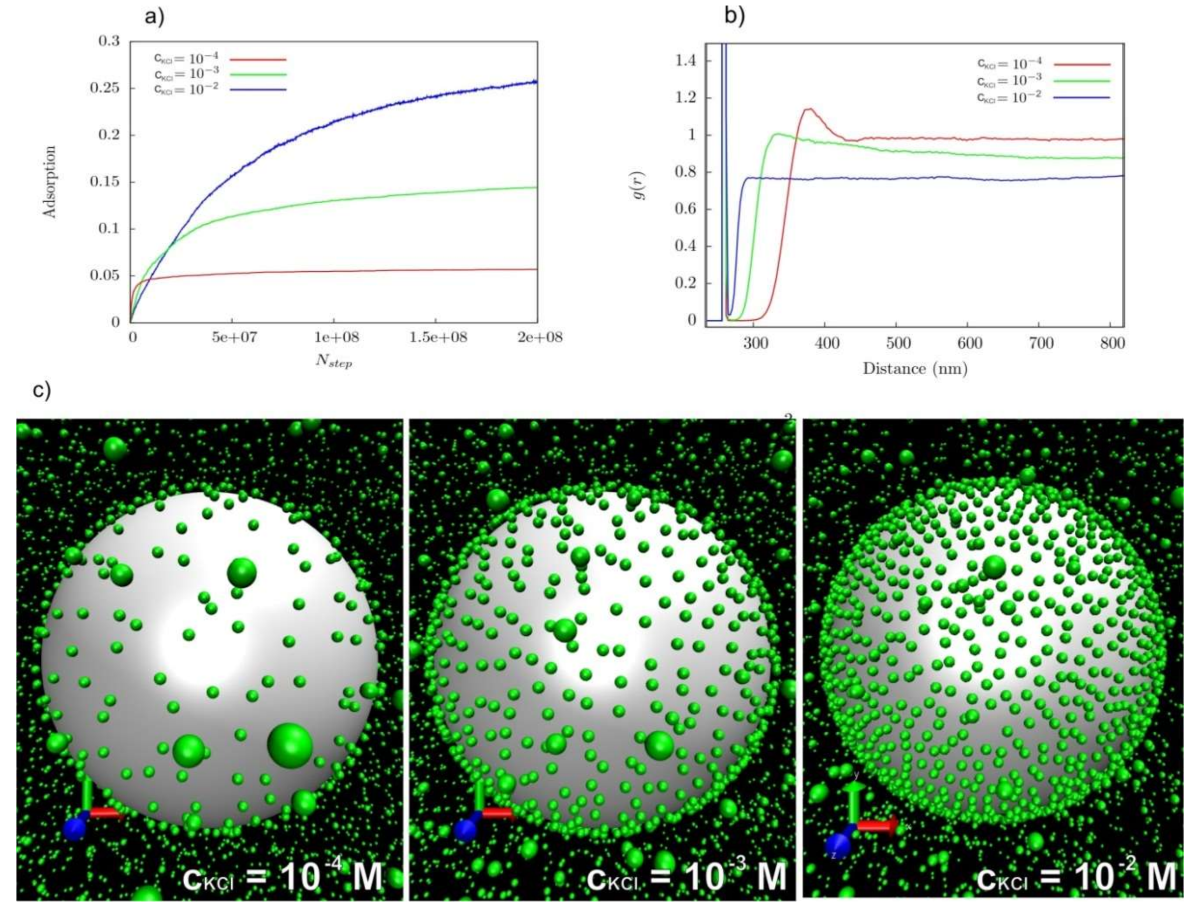

Figure 39: Density of surface coverage dependent for model SiO_2 – Y-TZP system on KCl concentration a) dependence of filing factor k on number of steps, b) radial distribution number and c) graphical representation.

The second simulation was performed using the experimental data on the Y-TZP – Y-TZP system; however, the spheres used in the simulation better apply to model the SiO_2 – Y-TZP system. With reference to Figure 40a the calculation showed that the k value exhibits larger values with an increased solids loading of the system, but still the initially predicted value of 0.91 is not reached. At an ionic strength of 0.0001 M the k equals 0.28. By increasing the ionic strength to 0.001 M nothing major happens and the k equals 0.32. The ionic strength of 0.01 M leads to a k of 0.45, which is the highest value obtained in the simulations. Since in our case the surface coverage factor k=0.91 was chosen, it seems that the nanoparticles in excess are positioned at some distance from the surface of the sub-micron-sized particles, as shown in Figure 40b. The figure shows the radial distribution function and how it depends on the ionic strength of the suspension. It can be observed that higher ionic strengths enable greater proximity of shell particles that were unable to come into hard contact with the surface of the core particles. Figure 40c is intended to visually represent the state in the colloidal system. One can clearly conclude that surface coverage is greater with ionic concentration of 10^{-2} M.

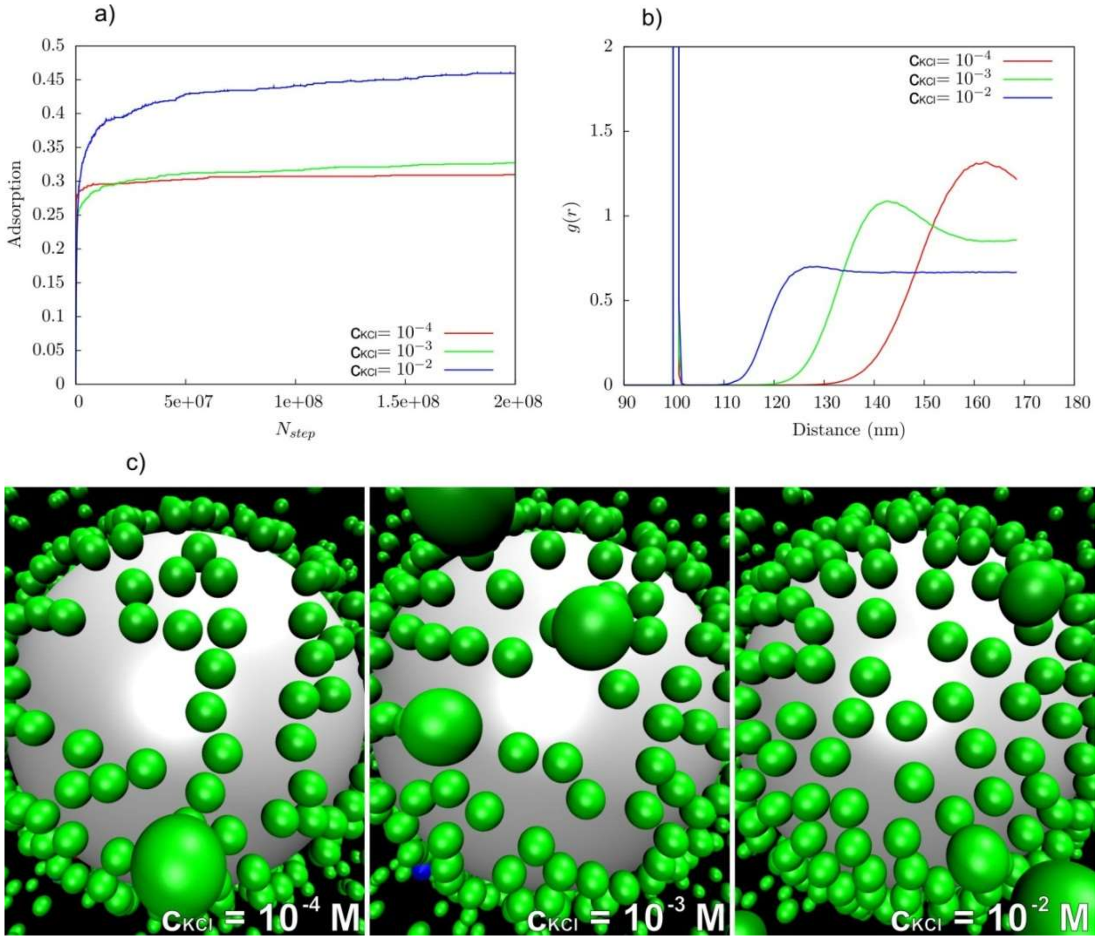

Figure 40: Density of surface coverage dependent on KCl concentration for model SiO2 – Y-TZP system showing in a) dependence of filing factor k on number of steps, b) radial distribution number and c) graphical representation.

The results of the simulation performed on both systems imply that surface-coverage factor k depends on the solids loading and on the ionic strength of the suspensions. However, at present no plausible conclusion can be given, but some preliminary experiments regarding influence of solid loading on r_H value are underway.

9 References

---

[1] Rouquerol, J. et al. Recommendations for the characterization of porous solids. *Pure & Appl. Chem.* **66**, 1739–1758 (1994).

[2] Čejka, J.; Bekkum, H.; Corma, A.; Schuth, F.; *Introduction to zeolite science and practice* (3rd revised edition, Elsevier B. V., 2007).

[3] Yanagisawa, T.; The Preparation of Alkyltriinethylaininonium–Kaneinite Complexes and Their Conversion to Microporous Materials, *Bulletin of the Chemical Society of Japan* **63**, 988–992 (1990).

[4] Beck, J. S.; Vartuli, J. C.; Roth, W. J.; Leonowicz, M. E.; Kresge, C. T.; Schmitt, K. D.; Chu, C. T-W.; Olson, D. H.; Sheppard, E. W.; McCullen, S. B.; Higgins, J. B.; and Schlenkert, J. L. A New Family of Mesoporous Molecular Sieves Prepared with Liquid Crystal Templates. *American Chemical Society* **114,** 10834–10843 (1992). doi:10.1021/ja00053a020

[5] Kresge C. T. et al. Ordered mesoporous molecular sieves synthesized by a liquid-crystal template mechanism, *Nature* 359, 710–712 (1992).

[6] Twigg, M. V.; Richardson. J. T. Theory and Applications of Ceramic Foam Catalysts. *Chem. Eng. Res. Design* **80**, 183–189 (2002).

[7] Adler, J. Ceramic Diesel Particulate Filters. *Int. J. Appl. Ceram. Tec.* **2**, 429–439 (2005).

[8] Hench, L. L. Bioceramics. *J. Am. Ceram. Soc.* **81**, 1705–1728 (1998).

[9] Colombo, P. Conventional and novel processing methods for cellular ceramics. *Phil. Trans. R. Soc. A* **324**, 109–124 (2006).

[10] Studart, A. R.; Gonzenbach, U. T.; Tervoort, E.; Gauckler, L. J. Processing routes to macroporous ceramics: A review. *J. Am. Ceram. Soc.* **89**, 1771–1798 (2006).

[11] Nichols, G.; Byard, S.; Bloxham, M. J.; Botterill, J.; Dawson, N. J.; Dennis, A.; Diart, V.; North, N. C.; Sherwood, J. D. A review of the terms agglomerate and aggregate with a recommendation for nomenclature used in powder and particle characterization. *J. Pharma. Sci.* **91**, 2103–2001, 13, 2109 (2002).

[12] Caruso, F. Nanoengineering of particle surfaces. *Adv. Mater.* **13**, No. 1, (2001).

[13] Davies, R.; Schurr, G. A.; Meenan, P.; Neslon, R. D.; Bergna, H. E., Brevett, C. A. S., Goldbaum, R. H., Engineered particle surfaces. *Adv. Mater.* **10**, 1264 (1998).

[14] Wu, Q.; Wang, Z.; Kong, X.; Gu, X.; Xue, G. A facile strategy for controlling the self assembly of nanocomposite particles based on colloidal steric stabilization theory. *Langmuir* **24**, 7778–7784 (2008).

[15] Somasundaran, P.; Chen, T-Y; Sarkar, D. A novel processing scheme for core-shell nanocomposites using controlled polymer adsorption. *Mat. Res. Innovat.* **2**, 325–327 (1999).

[16] Wu, Q.; Wang Z.; Kong X.; Gu X.; Xue G. A facile strategy for controlling the self assembly of nanocomposite particles based on colloidal steric stabilization theory. *Langmuir* **24**, 7778–7784 (2008).

[17] Gouy, M. Sur la constitution de la charge électrique à la surface d'un electrolyte. *J. de Phys.*, 457–468 (1910).

[18] Fengqiu, T., Xiaoxian, H.; Yufng, Z.; Jingkun, Effect of dispersants on surface chemical properties of nano-zirconia suspension. *Ceramics international* **26**, 93–97 (2000).

[19] Lyklema, H. Molecular interpretation of electrokinetic potential. **15**, 125–130 (2010)

[20] Israelachvili, J. N. *Intermolecular and surface forces* (Academic Press Limited 2nd Edition).

[21] Min, Y.; Akbulut, M.; Kristiansen, K.; Golan, Y.; Israelachvili, J. The role of interpartcile and external forces in nanoparticle assembly. *Nature materials* **7**, 527–538 (2008).

[22] Hogg R.; Healy, T. W.; Fuerstenau D. W. Mutual coagulation of colloidal dispersions, *Trans. Faraday Soc.* **62**, 1638–1651 (1966).

[23] Bleier, A.; Matijevič, E. Heterocoagulation Part3 – Interactions of polyvinyl chloride latex with ludox HS silica. *Journal of chemical society, Faraday transactions 1: Physical chemistry in condensed phases* **74**, 1346–1359 (1978).

[24] Bergstrom, L. Hamaker constants of inorganic materials. *Adv. Coll. Inter. Sci.* **70**, 125–169 (1997).

[25] Piechowiak, M. A. et al. Oppositely Charged Model Ceramic Colloids: Numerical Predictions and Experimental Observations by Confocal Laser Scanning Microscopy. *Langmuir* **26**, 12540–12547 (2010).

[26] Trefalt, G.; Tadić, B.; Kosec, M. Formation of colloidal assemblies in suspenisons for Pb(Mg1/3Nb2/3)O3 synthesis: Monte carlo simulation study. *Soft matter* **7**, 5566 (2011).

[27] Lange F. F. Powder Processing Science and Technology for Increased Reliability. *J. Amer. Ceram. Soc.* **72**, 3–15 (1989).

[28] Aksay, I. A.; Lange, F. F.; Davis, B. I. Uniformity of AI20,-ZrO2 Composites by Colloidal Filtration. *J. Amer. Ceram. Soc.* **66**, C190–C192 (1983).
[29] Lange F. F., Shape forming of ceramic powders by manipulating the interparticle pair potential. *Chemical Engineering science* **6**,3011–3020 (2001).

[30] James S. R. Introduction to the principles of Ceramic Processing (John Wiley & Sons, 1988).

[31] Takao Y. et al. Processing defects and their relevance to strength in alumina ceramics made by slip casting. *J. Eur. Ceram. Soc.* **20**, 389–395 (2000).

[32] Maleksaeedi S.; Paydar, M. H.; Saadat, S.; Ahmadi, H. In situ vibration enhanced pressure slip casting of sub-micrometer alumina powders. *J. Eur. Ceram. Soc.* **28**, 3059–3064 (2008).

[33] Fennellz, T.J.; Reed, J. S. Mechanics of pressure slip casting. *J. Amer. Cer. Soc.* **55**, 264–268 (1972).

[34] Yu, B. C.; Biesheuvel, P. M.; Lange, F. F. Compact formation during colloidal isopressing. *J. Am. Ceram. Soc.* **85**, 1456–60 (2002).

[35] Kosmač, T. The densification and microstructure of Y-TZP ceramics formed using the hydrolysis-assisted solidification process. *J. Amer. Cer. Soc.* **88**, 444–1447 (2005). doi:10.1111/j.1551-2916.2005.00333.x.

[36] Tallon, C; Limacher, M.; Franks, G. V. Effect of particle size on the shaping of ceramics by slip casting. *J. Eur. Ceram. Soc.* (2010).

[37] Renger, C.; Kuschel, P.; Rheology studies on highly filled nano-zirconia suspensions. *Journal of European ceramic society* **27**, 2361–2367 (2007).

[38] Sigmund, W. M. Novel powder-proccesing methods for advanced ceramics. *Journal of American ceramic society* **83**, 1557–1574 (2000).

[39] Tallon, C.; Limacher, M.; Franks, G. V. Effect of particle size on the shaping of ceramics by slip casting. *J. Eur. Ceram. Soc.***30**, 2819–2826 (2010).

[40] Raghupathy, B. P. C.; Binner, J. G. P. Spray granulation of nanometric zirconia particles. *J. Am. Ceram. Soc.* **94**, 42–48 (2010). doi: 10.1111/j.1551-2916.2010.04019.x

[41] Exner, H. E. Principles of Single Phase Sintering. *Reviews in Powder Metallurgy and Physical Ceramics* **1**, 1–251 (1979).

[42] Reed, J. S. *Introduction to the Principles of Ceramic Processing* (Wiley-Interscience, New York, 1988, p. 87).

[43] Kang, S-J. L. *Sintering: densification, grain growth and microstructure* (Elsevier Butterworth-Heinemann, 2005, Netherlands).

[44] Rosolowaki, J. H.; Greskovich, C. Theory of the dependence of densification on grain growth during intermediate stage sintering. *J. Amer. Ceram. Soc.* **58**, 177–182 (1975).

[45] Coble, R. L. Sintering Crystalline Solids. I. Intermediate and Final State Diffusion Models. *J.Appl.Phys.* **32**, 787 (1961).

[46] McAfee, R. J. *A Study of Microstructural Evolution During Sintering Using Tessllation*, (Ph. D. Thesis, Univ. of Pittsburgh, 2004).

[47] Schuth F.; Kenneth, S. S. W. *Handbook of porous solids, Volume 1,* (Wiley-vch Verlag GmbH, 2002).

[48] Hirata, Y.; Hara, A.; Aksay, I. A. Thermodynamics of powder compact. *Ceram. Int.* **35**, 2667–2674 (2009).

[49] Ashby, M. F. A first report on sintering diagrams. *Acta metallurgica*, **22**, 275–289 (1974).

[50] Swinkles, F. B.; Ashby, M.F. A second report on sintering diagrams. *Acta Metallurgica* **29**, 259–281 (1981).

[51] Theunissen, G. S. A. M.; Winnubst, A. J. A.; Burggraff, A. J. Sintering kinetics and microstructures development of nanoscale Y-TZP ceramics. *J. Eur. Ceram. Soc.* **11**, 315–324 (1993).

[52] Young, W. S.; Cutler, I. B. Initial sintering with constant heating rate. *J. Amer. Cer. Soc.* **53**, 659–663 (1970).

[53] Binner, J.; Vaidhyanathan, B. Processing of Bulk nanostructural ceramics. *J. Eur.Ceram. Soc.* **28**, 1329–1339 (2008).

[54] Chang, H. N.; Pan, J. Sintering of particles of different sizes. *Acta Materialia* **55**, 813–824 (2007).

[55] Fang, Z. Z.; Wang, H. Densification and grain growth during sintering of nanosized particles. *International materials review* **53**, 326–352 (2008).

[56] Groza J. R. Nanosintering. *Nanostructured materials* **12**, 987–992 (1999).

[57] Groza, J. R.; Dowding, R. J. Nanoparticulate materials densification. *Nanostructured materials* **7**, 749–768 (1996).

[58] Chaim, R. Densification mechanisms in spark plasma sintering of nanocrystalline ceramics. Mater. *Science and Engineering A* **25**, 443 (2007).

[59] Harris, K. E.; Singh, V. V.; King, A. H. Grain rotation in thin films of gold. *Acta materialia* **46**, 2623 (1998).

[60] Li, Y.; Xu, Z. H.; Wang, R. In Situ Observation of Nanograin Rotation and Deformation in Nacre. *Nano Letters* **6**, 2301–2304 (2006).

[61] Gablekov, S. V.; Tarasov, R. V.; Mironova, A. G. Change in poresructure of Ytrria – stabilized zirconia during sintering. *Powder metal. Metal ceram.* **50**, 151–156 (2011).

[62] Schmidt, S. A.; Nettleship, I. The effect of coarse particles on the microstructural evolution of porous alumina sintered at 1375 °C. *J. Eur. Cer. Soc.* **24**, 2741–2747 (2004).

[63] Messing, G.L.; Onoda, G. Y. Inhomogeneity – Packing density relations in binary powders, *J. Amer. Ceram. Soc.* **61**, 1–5 (1978).

[64] Smith, J. P.; Messing, G. L.; Sintering of bimodally distributed alumina powders. *J. Amer. Ceram. Soc.* **67**, 238–242 (1988).

[65] Yeh, T. S.; Sacks, M. D. Effect of particle size distribution on the sintering of alumina. *J. Am. Ceram. Soc.* **71**, C484–C487 (1988).

[66] Shiau, F. S.; Fang, T. T.; Leu, T. H. Effect of particle-size distribution on the microstructural evolution in the intermediate stage of sintering. *J. Am. Ceram. Soc.***80**, 286–290 (1997).

[67] Petersson, A.; Agren, J. Sintering shrinkage of WC-Co materials with bimodal grain size distibutions. *Acta materialia* **54**, 111–118 (2005).

[68] Ravi, B. G.; Chaim, R. Sintering of bimodal alumina powder mixtures with nanocrystalline component. *Nanostructured materials* **11**, 853–859 (1999).

[69] Ostrowski, T.; Rodel, J. Evolution of mechanical properties of porous alumina during free sintering and hot pressing. *J. Am. Ceram.* Soc. **82**, 3080–3086 (1999).

[70] Exner, H.E.; Muller, C. Particle Rearrangement and Pore Space Coarsening During Solid-State Sintering. *J. Am. Ceram. Soc.* **92**, 1384–1390 (2009).

[71] Kingery W. D.; Francois, B. Sintering of Cristalline Oxides, I. Interaction between Grain Boundaries and Pores, in *Sintering and Related Phenomen.* Edited by G. C. Kuczynski, N. A. Hooton, and G. F. Gibbon. Gordon Breach, New York, 471–98 (1967).

[72] Slamovich E.; Lange, F. F. Densification of Large Pores: II, Driving Potentials and Kinetics. *J. Am. Ceram. Soc.* **76,** 1584–90 (1993).

[73] Flinn, B. D.; Bordia, R. K.; Zimmermann, A.; Rodel, J. Evolution of defect size and strength of porous alumina during sintering. *J. Am. Ceram. Soc.* **20**, 2561–2568 (2000).

[74] Colombo, P. Conventional and novel processing methods for cellular ceramics. *Phil. Trans. R. Soc. A* **324**, 109–124 (2006).

[75] Ramay, H. R.; Zhang, M. Preparation of porous hydroxyapatite scaffolds by combination of the gel-casting and polymer sponge methods. *Biomaterials* **24**, 3293–3302 (2003).

[76] Weber, J. N.; White, E. W. Fabrication of porous hydroxyapatite ceramics by microwave processing. *Science* **176**, 922–924 (1972).

[77] Colombo, P.; Bernardo, E.; Biasetto, L. Novel Microcellular Ceramics from a Silicone Resin. *J. Am. Ceram. Soc.* **87**, 152–154 (2004).

[78] Studart, A. R.; Gonzenbach, U. T.; Tervoort, E.; Gauckler, L. J. Processing Routes to Macroporous Ceramics: A Review. *J. Am. Ceram. Soc.* **89**, 1771–1798 (2006).

[79] Colombo, P. In Praise of Pores. *Science* **322**, 381 (2008).

[80] Deng, Z.Y.; Yang, J. F.; Beppu, Y.; Ando, M.; Ohji, T. Effect of Agglomeration on Mechanical Properties of Porous Zirconia Fabricated by Partial Sintering. *J. Am. Ceram. Soc.* **85**, 1961–1965 (2002).

[81] Kosmac, T.; Andrzejczuk, M.; Kurzydlowski, K. J. *Ceramic Engineering and Science Proceedings* **27** (2008).

[82] Hardy, D.; Green, D. J. Mechanical properties of a partially sintered alumina. *J. Eur. Ceram. Soc.* **15**, 769–775 (1995).

[83] Li G.; Jiang Z.; Jiang A.; Zhang L. Strengthening of porous Al2O3 ceramics through nanoparticle addition. *Nanostructured materials* **8**, 749–754 (1997).

[84] Kritikaki, A.; Tsetsekou, A. Fabrication of porous alumina ceramics from powder mixtures with sol-gel derived nanometer alumina: effect of mixing method. *J. Eur. Ceram. Soc.* **29**, 1603–1611 (2009).

[85] Volceanov, E.; Volceanov, A.; Stoleriu, S. Assessment on mechanical properties controlling of alumina ceramics for harsh service conditions. *J. Eur. Ceram. Soc.* **27**, 759–762 (2007).

[86] Wakamatsu, M.; Ishida, S.; Takeuchi, N.; Hattori, T. Effect of Firing Atmosphere on Sintered and Mechanical Properties of Vanadium-Doped Alumina. *J. Am. Ceram. Soc.* **74**, 1308–11 (1991).

[87] Jayaseelan, D. D.; Kondo, N.; Brito, M. E.; Ohji, T. High-Strength Porous Alumina Ceramics by the Pulse Electric Current Sintering Technique. *J. Am. Ceram. Soc.* **85**, 267–69 (2002).

[88] Perko, S.; Dakskobler, A.; Kosmac, T. High-performance nanostructured ceramics, *J. Amer. Cer. Soc* **93**, 2499–2502 (2010).

[89] Luo, J.; Stevens, R. Porosity – dependence of elastic moduli and hardness of 3Y-TZP ceramics. *Ceramics International* **25**, 281–286 (1999).

[90] Roberts, A. P.; Garboczi, E. J. Elastic properties of model porous ceramics. *J. Am. Ceram. Soc.* **83**, 3041–3048 (2000).

[91] Granger, G. B.; Guizard, C. Apparent activation energy for the densification of a commercially available granulated zirocnia powder. *J. Am. Ceram. Soc.* **90**, 1246–1250 (2007).

[92] Morrell, R. *Biaxial flexural strength testing of ceramic materials* (National physical laboratory Teddington, Middlesex, UK, ISSN 1368–6550, 2007).

[93] Shetty, D. K.; Rosenfiled, A. R.; McGuire, P.; Bansal, G. K.; Duckworth, W. H. Biaxial flexure tests for ceramics. *Am. Ceram. Soc. Bull.* **59**, 1193–1197 (1980).

[94] Hidber, P. C.; Graule, T. J.; Gauckler, L. J. Citric acid – a dispersant for aqueous alumina suspensions. **79**, 1857–1867 (1996).

[95] Fischer, M. L.; Colic, M.; Rao, M. S.; Lange, F. F. Effect of silica nanoparticle size on the stability of alumina/silica suspensions. *J. Amer. Cer. Soc.* **84**, 713–718 (2001).

[96] Yates, P. D.; Franks, G. V.; Biggs, S.; Jameson, G. J. Heteroaggregation with nanoparticles: effect of particle size on optimum particle dose. *Colloids and Surfaces A* **255**, 85–90 (2005).

[97] Rosolowski, J. H.; Greskovich, C. Theory of the dependence of densification on grain growth during intermediate stage sintering. *J. Amer. Cer. Soc.* **58**, 177–182 (1974).

[98] Kim, S.; Lee, K. S.; Zachariah M. R.; Lee, D. J. *Colloid Interface Sci.* **344**, 353–361 (2010).

[99] Heermann, D. *Computer Simulation Methods in Theoretical Physics* (Springer-Verlag, Berlin, 1990).

[100]Allen M. P.; Tildesley, D. J. *Computer Simulation of Liquids* (Claredon Press, Oxford, 1989).

10 Index of figures

11 Index of tables

Personal bibliography for the period of the doctoral study (2009-2012)

Articles and other component parts

Original scientific article

[1] Kosmač, T.; Andrejczuk, M.; Perko S. The fabrication and properties of biscuit-sintered Y-TZP ceramics for dental applications. *Key eng. mater.* **409**, 342–345 (2009). [COBISS.SI-ID 22607911] tipologija 1.08 -> 1.01

[2] Perko, S.; Dakskobler, A.; Kosmač T. High-performance porous nanostructured ceramics. *J. Am. Ceram. Soc.* **93**, 2499–2502 (2010). doi: 10.1111/j.1551-2916.2010.03835.x. [COBISS.SI-ID 23812391]

[3] Perko, S.; Dakskobler, A.; Kosmač, T. The densification and strength of porousY-TZP materials with a bimodal particle size distribution for dental applications. *J. Eur. Ceram. Soc.* (2012). doi:10.1016/j.jeurceramsoc.2012.02.001

Published scientific conference contribution abstract

[4] Kosmač, T.; Andrejczuk, M.; Perko, Izdelava in lastnosti delno porozne cirkonijeve (Y-TZP) keramike za zobno protetiko. V: ISKRA, Jernej (ur.), MILOŠEV, Ingrid (ur.). *Dan mladih raziskovalcev 2009*. Ljubljana: Institut "Jožef Stefan", 2009, 1 str. [COBISS.SI-ID 22446119]

[5] Perko, S.; Dakskobler, A.; Kosmač T. Preparation and mechanical properties of porous Y-TZP ceramics for dental applications. V: JENKO, Monika (ur.). 17. konferenca o materialih in tehnologijah, 16.–18. november 2009, Portorož, Slovenija *Program in knjiga povzetkov*. (Inštitut za kovinske materiale in tehnologije, Ljubljana, 2009, str. 33) [COBISS.SI-ID 23126823]

[6] Perko, S.; Dakskobler, A.; Kosmač T. Mechanical properties of porous Y-TZP core-shell nanocomposites. V: SRDIĆ, Vladimir V. (ur.), RANOGAJEC, Jonjaua (ur.). The Eighth Students' Meeting Processing and Application of Ceramics, SM 2009, December 2–5, 2009, Novi Sad, Serbia. *Programme and book of abstracts*. (Faculty of Technology, University of Novi Sad, 2009, str. 49). [COBISS.SI-ID 23437351]

[7] Perko, S.; Dakskobler, A.; Kosmač T. High performance porous nanostructured ceramics. V: 11th International Conference on Ceramic Processing Science Zurich, Switzerland, 29th August–1st September, 2010. *ICCPS-11*. [S. l.: s. n.], 2010. [COBISS.SI-ID 23953191]

[8] Perko, S.; Dakskobler, A.; Kosmač T. Biscuit-sintered zirconia ceramics for dental applications. V: *Meeting IADR general session, Barcelona, July 14* Barcelona: *17, 2010.* (International Association for Dental Research, Barcelona, 2010). [COBISS.SI-ID 23952423]

[9] Perko, S.; Dakskobler, A.; Kosmač T. High-performance porous Y-TZP ceramics for dental applications. V: JENKO, Monika (ur.). 18. konferenca o materialih in tehnologijah, 15. –17. november 2010, Portorož, Slovenija *Program in knjiga povzetkov*. (Inštitut za kovinske materiale in tehnologije, Ljubljana, 2010, 34). [COBISS.SI-ID 24309031]

[10] Perko, S.; Dakskobler, A.; Kosmač T. Priprava in mehanske lastnosti delno porozne cirkonijeve (Y-TZP) keramike za zobno protetiko. V: KUŠČER, Danjela (ur.), PERC, Branka (ur.). 4. Dan mladih raziskovalcev KMBO, Ljubljana, Slovenija, 11. 2. 2010. *Program in povzetki*. (Institut "Jožef Stefan", Ljubljana, 2010, str. 15). [COBISS.SI-ID 23435815]

[11] Perko, S.; Dakskobler, A.; Kosmač T. Biscuit - sintered zirconia ceramics for dental applications. V: KALUŽA, Boštjan (ur.), ELERŠIČ, Kristina (ur.), POGORELC, Bogdan (ur.), ŠETINA, Barbara (ur.), VAHČIČ, Mitja (ur.). 2. študentska konferenca Mednarodne podiplomske šole Jožefa Stefana *Zbornik prispevkov*. (Mednarodna podiplomska šola Jožefa Stefana, Ljubljana, 2010, str. 62). [COBISS.SI-ID 23759655]

[12] Perko, S.; Dakskobler, A.; Kosmač T. Moderately porous Y-TZP ceramics for dental applications. V: 12th Conference of the European Ceramic Society, June 19–23, 2011, Stockholm, Sweden. *ECerS XII*. [S. l.]: ECERS, 2011. [COBISS.SI-ID 25415719]

[13] Perko, S.; Dakskobler, A.; Kosmač T. Sensification and strength of porous Y-TZP ceramics with a biomodal prticle size distribution. V: International Conference on Sintering 2011, August 28–September 1, 201, Jeju, Korea. *Meeting guide & abstracts*. [S. l.: s. n.], 2011, str. 38. [COBISS.SI-ID 25116199]

[14] Perko, S.; Dakskobler, A.; Kosmač T. Densification and strength of porous Y-TZP ceramics. V: SRDIĆ, Vladimir V. (ur.), MITOSERIU, Liliana (ur.). The Ninth Students' Meeting and Application of Ceramics, SM-2011 [and] The Second Early Stage Researchers Workshop, COST MP0904,16–18 November 2011, Novi Sad, Serbia. *Programme and book of abstracts*. (Faculty of Technology, University of Novi Sad, 2011, str. 60). [COBISS.SI-ID 25415463]